Single Electron Transistors and Carbon Nanotube Double Quantum Dots

Dissertation for the degree of Master of Science

Thomas Bebis

June 2006

Ir. S. Sapmaz
Prof. dr. ir. L.P. Kouwenhoven

Kavli Institute of Nanoscience
Quantum Transport Group
Delft University of Technology

Abstract

Carbon nanotubes have attracted a great deal of attention during the past fifteen years since their discovery. Their unique physical properties make them promising candidates for a number of future applications, such as quantum computing and molecular optoelectronic devices. A lot of the physics concerning nanotubes however, like orbital and spin lifetimes, have this far remained elusive. As theory predicts long orbital and spin lifetimes for nanotubes, experiments to determine these quantities have attracted scientific interest.

Most of the schemes employed so far in other systems to measure such quantities rely on the ability to control single electrons. This is typically done by confining electrons in single or double quantum dots and then performing pulse experiments. Based on the theoretical predictions mentioned above we expect that the measurable current for carbon nanotube double dot systems could be too small to measure through dc transport measurements. Single Electron Transistors, the most sensitive electrometers known presently, are however able to measure even a single electron charge tunneling through the dot. They can therefore be used to perform charge instead of transport measurements measurements on carbon nanotube double quantum dots.

We report on the reproducible fabrication and characterization of Single Electron Transistors (SETs) and Carbon Nanotube Double Quantum Dots with narrow top gates. The Single Electron Transistors can couple electrostatically to the double quantum dots to perform charge sensing. Charge detection however is found to depend critically on the SET position and proximity to the nanotube dots.

Contents

Chapter 1

Introduction

This report is written in partial fulfilment of the requirements for the degree of Master of Science from the Kavli Institute of Nanoscience at the Delft University of Technology. Relevant research was performed in the Quantum Transport Group. The work was supervised by Ir. S. Sapmaz and was conducted in the group of prof. dr. ir. L.P. Kouwenhoven.

1.1 Motivation for this work

The semiconductor industry has been driven in the past decades by Moore's law, which states that the computing capacity of a computer chip doubles roughly every two years thus leading to a proportionate increase in speed and decrease in feature size. This staggering prediction has held true till today, but it is expected to break down in the coming decade. Clever engineering and exotic materials do not seem to be enough to counterbalance the quantum mechanical effects that dominate structures with feature sizes comparable to the electron's Fermi wavelength. Richard Feynman, in his famous talk "There is plenty of room at the bottom", was the first to envision an era of nanoscience and in 1982 even showed that quantum mechanical systems could be used as computational devices. A few years later David Deutsch described a universal quantum computing scheme while Peter Shore successfully solved a difficult problem concerning factorization that was relevant to a quantum computer's operation.

These two combined developments have sparked an intense competition, with roughly two main parts: The first involves the creation of a quantum computer able to work with a large number of information bits, so called qubits; the second involves the study of how small groups of molecules, or even single molecules, conduct electricity. Molecular Electronics deals exactly with this issue: the formulation of a theory for conduction that includes individual electron levels of a single/few atom(s).

The research in this thesis is relevant to both: on one hand it involves single molecules, such as carbon nanotubes (CNTs) (Fig. 1.1) and their energy levels; on the other hand it deals with quantum phenomena arising at small length scales and ultra-low temperatures and has potential applications for quantum computing.

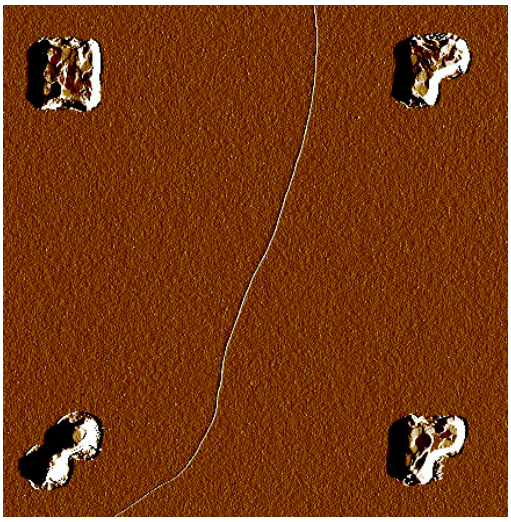

Figure 1.1: An AFM image of a carbon nanotube grown on a silicon wafer. The four metal markers at the corners are used for electron beam aligning.

1.2 Quantum Computation

If a classical bit is represented as either 0 or 1 a qubit can be represented by $|\Phi\rangle = \alpha|0\rangle + \beta|1\rangle$, a superposition of the two (classical) states in which α^2 and β^2 give the probability that a measurement returns the value $|0\rangle$ or $|1\rangle$ respectively. For two qubits, we can have states $|00\rangle$, $|01\rangle$, $|10\rangle$ or $|11\rangle$ and the superposition of these states would be represented by $|\Phi\rangle = \alpha|00\rangle + \beta|01\rangle + \gamma|10\rangle + \delta|11\rangle$: an operation acting on this superposition of states would act on 4 states. Scale this up to N states and one ends up with operations acting on 2^n states, and exponential increase in operation power.

In principle, any two-level quantum system could operate as a quantum computer. For carbon nanotube molecules, of particular relevance is the electron spin. If electron spin is to be used then as a qubit it would be desirable that these "up" and "down" states are relatively stable in time. This means that an electron should be able to spend enough time in each state so that the operation carried out is fully performed before a transition to another state occurs.

1.3 Carbon Nanotubes and Quantum Computation

Theoretical calculations for carbon nanotubes (cNTs) [1] predict very long spin and orbital lifetimes. More specifically, most of natural carbon is without nuclear spin. In addition, spin-orbit coupling is weak in nanotubes due to carbon's low atomic number. Some of the mechanisms responsible for spin decoherence are therefore very weak in nanotubes. As a result, nanotubes are considered ideal candidates for quantum computation based on spin. One of the further goals of this project was to pinpoint more precisely how long these lifetimes can be.

Other than this, nanotubes are very interesting materials in virtue of their mechanical properties: they are long, flexible and very strong molecules [2]. Due to their robustness and relatively large sizes for single molecules, which can be of the order of many microns, they have therefore been proposed as candidates for various molecular electronics devices: they have been used as molecular wires [3], room temperature Field-Effect-Transistors (FETs) [4] and as optoelectronic devices [5]. To this end, it is interesting by itself to study how current flows through these molecule and try to extract useful characteristics about the energy levels through which electrons move.

1.4 Carbon Nanotube Quantum Dots

To be able to distinguish electronic states within a nanotube one can form quantum dots of them. These are short areas of the nanotube that are separated from the rest of the tube by tunnel barriers. These barriers are usually formed by applications of large voltages on narrow top gates, see Fig. 1.2. These voltages spatially deplete electrons from the nanotube segment that lies beneath and make it energetically more difficult for them to pass through: an electron is essentially confined to the area between the tunnel barriers, this region being called a Quantum Dot (QD). Given enough time and under proper conditions (no *Coulomb Blockade*) electrons will eventually tunnel in/out of the dot and provide a measurable current. A large tunneling rate provides larger measurable current while smaller tunneling rates leads to smaller currents, with a present bound on the smallest resolvable current being approximately 15 fA.

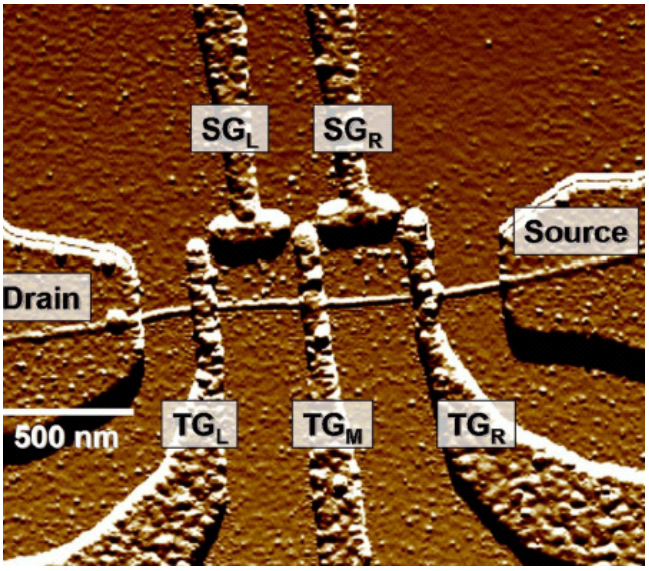

Figure 1.2: A carbon nanotube double quantum dot. The nanotube is covered on opposite sides by Palladium source and drain electrodes. The middle top gates deplete electrons on the tube below them, thus forming two isolated regions on the tube, dot 1 and dot 2. Adapted from [6].

1.5 Acknowledgements

I feel the need to express my gratitude to certain people without whose help and support none of this would have been possible. First of all I would like to thank my supervisor in the group, Sami Sapmaz. I appreciated your desire to always wanting me to understand exactly what we were trying to do and your constant support during the long fabrication and testing period. Although we were alone in fabrication somehow you always made up for the lack of others. Our discussions about Greek customs, mythology, Turkish food and your interest in learning new things is very rare. I wish you the best in whatever you do after you receive your PhD. My thanks also go to Fleur for sharing the student room with me and for the interesting discussions. A thanks is due to Floris from the next door office for always making things a bit lighter! I would also like to thank Peter Hadley for useful discussions related to the project. Finally a big thanks goes to Leo for taking me in the group with an open heart; I don't think it is easy to find such a group that offers such optimum conditions for research as QT elsewhere in the world. I believe your way of running the group is an example to others.

On a more personal note, I would like to thank some of the Greek community members who have made life in Delft and the much maligned spaceboxes more livable, particularly during my second year. A big thanks goes to Thanasis Tsitouras, Kyriakos Nathanail, Dimosthenis Manias and Charis Sinos for some very nice philosophical after-hour discussions, some excellent cooking sessions and a lot of fun.

My deepest thanks goes to those who have unerringly supported me in my long study journey this far: my two parents and brother who have provided me with all means necessary to pull through the difficulties of the past years. $Ευχαριστω\ για\ ολα$! Then on an almost equal par stand my teachers. I've been fortunate to have been tutored by very special people over the years, all the way from elementary school till now and I would not have been the same without them. $Ευχαριστω\ για\ το\ φως$.

Finally I want to thank my Eva-Nina, my *poli-polo*, for being there for me during the past year. Life at Delft was really not the same after you. You know you have all my love!

$Θωμας$

Chapter 2

Carbon Nanotubes

In this chapter some of the relevant theory of carbon nanotubes is discussed. Carbon nanotubes are extremely thin (diameters of ~ 1 nm) and hollow macromolecular systems. They were first discovered in 1991 by Sumio Iijima and produced massively in single-wall form a few years later by techniques developed by Richard Smalley. Their unusual physical and chemical properties quickly captured the imagination of the scientific community. Depending on how they are rolled up they can be made to be either metals or semiconductors, while their large aspect ratios make them ideal one-dimensional systems.

2.1 Graphene Band Structure

A single wall carbon nanotube, see Fig. 1.1, can be thought of as a two-dimensional graphene sheet rolled up to form a seamless, hollow cylinder. Graphene is a sheet of carbon atoms where the carbon atoms are arranged in a 2D hexagonal lattice. Now, every carbon atom has four electrons to share. Of these, three electrons per atom are responsible for sp^2 hybridized σ-bonds with three neighboring atoms while the fourth electron occupies a p_z orbital situated vertically to the graphene sheet. These p_z orbitals among neighboring carbon atoms overlap to form weak π-bonds and it is these orbitals that are responsible for electron conduction as electrons hop through different lattice atoms on a nanotube.

The process of rolling up a graphene sheet to make CNTs can be mathematically described by a so-called *chiral* vector. This chiral vector $\overrightarrow{C}$ can be expressed on the basis unit vectors a_1 and a_2 of graphene as

$$\overrightarrow{C} = n\overrightarrow{a_1} + m\overrightarrow{a_2} \tag{2.1}$$

with n, m integers. By joining different beginnings and ends for the chiral vector one can get nanotubes with different properties. Depending on n and m therefore three distinct geometries arise: armchair, zigzag or chiral nanotubes (Figure 2.1) where the nanotube diameter is given by

$$d = C/\pi = (\alpha/\pi)(\sqrt{n^2 + m^2 + nm}) \tag{2.2}$$

where a = 0.245 nm and C being the circumference of the tube. The dispersion

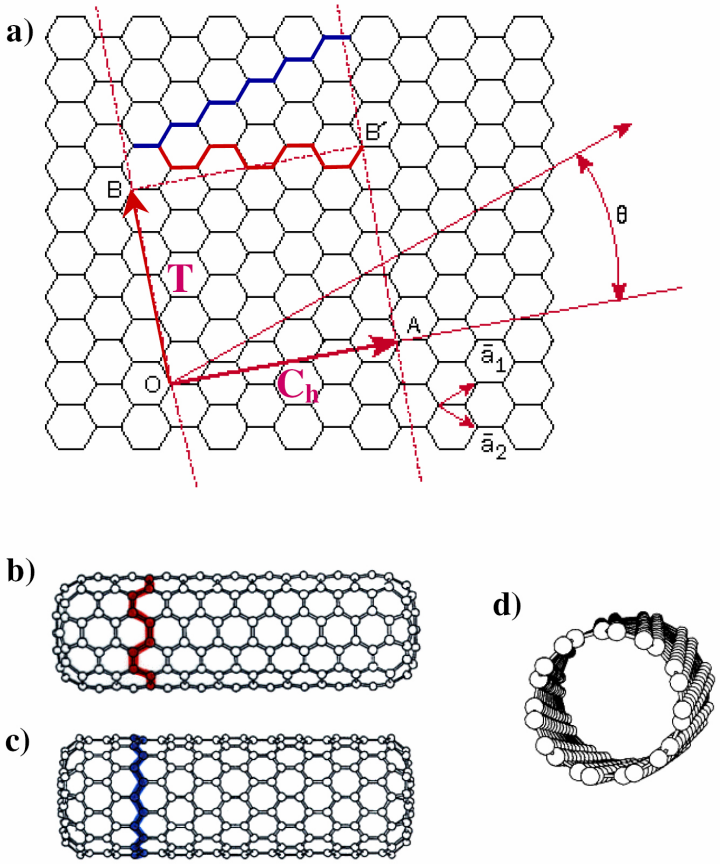

Figure 2.1: a) The process of rolling up a graphene sheet. For different chiral vectors **C** a variety of nanotubes with different properties occur. Nanotubes can turn out as either *armchair* (b), *zigzag* (c) or *chiral* (d). Reproduced from [7].

relation for electrons in a graphene sheet can be calculated using a tight-binding model to be

$$E_{graphene} = \pm\gamma_0[1 + 4cos(\sqrt{3}k_y\alpha/2)cos(k_x\alpha/2) + 4cos^2(k_x\alpha/2)]^{1/2} \qquad (2.3)$$

where γ_0 is the C-C overlap integral, or more simply the bond strength. The two resulting bands, a bonding (*valence*) and an anti-bonding (*conduction*) one, are the consequence of having two atoms per graphene unit cell. These two bands cross at 6 points in reciprocal space which happen to coincide with the corners of the first Brillouin zone, or stated differently, the energy at these six points equals the fermi energy E_F. Of these six so called "K-points" only two are inequivalent, meaning that one cannot reach all six K-points by starting from a single one. Instead, some of the K-points are reachable by translations starting from one K-point while the rest are only reachable from a different K-point. All six points however can be reached starting from two different K-points. This is a result of the two inequivalent atom sites in the graphene lattice unit cell.

2.2 Electronic Structure and Properties of CNTs

To go from the graphene band structure to that of a nanotube, we simply impose periodic boundary conditions to the electron wave vector in the direction of the circumference of the tube

$$\overrightarrow{C} \cdot \overrightarrow{k} \;=\; \pi d k_{\perp} \tag{2.4}$$

Now each band of graphene splits up into sets of one-dimensional subbands. The allowed energy states for electrons in nanotubes are therefore represented by cuts through the graphene bands. These cuts are spaced by $\Delta k_{\perp} = 2/\mathrm{d}$ so that for small diameter tubes ($\backsim$1 nm) only a few wave vectors exist in the circumferential direction.

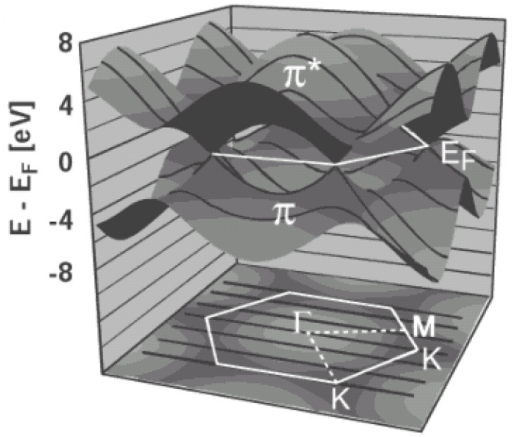

Figure 2.2: Band structure of a 2-D graphene sheet. The two bands cross at six so called K-points. Below (white) is the first Brillouin zone. For this particular nanotube the cuts imposed by periodic conditions cross through the K-points. This nanotube is therefore metallic. Reproduced from [8].

Depending on the integers n and m, see Eq. 2.4, it may happen that these "cuts" imposed by the periodic conditions mentioned above pass through the K-points. When that happens the tube is metallic (n = m): the usual graphene conical bandstructure reduces to linear dispersion relations at k_F with two modes present at k_F and -k_F. One branch has a positive while the other has a negative slope. These represent states for right and left movers respectively. If however no cuts pass through a K-point the tube is considered semiconducting (n - m $\neq$ 3i), see Fig. 2.3. This means that an energy gap now opens up at the Fermi energy. We are mostly interested in what happens at E_F because it is these electrons that are responsible for conduction.

Concerning phonons, vibrations of the rolled-up graphene lattice, a very crude first approximation is that generally scattering between states is suppressed. To scatter from states at one K-point to another K-point, a large change in momentum of $2k_F$ is required for an electron. An acoustical phonon would then have to possess an energy of about 100 meV, much larger that kT

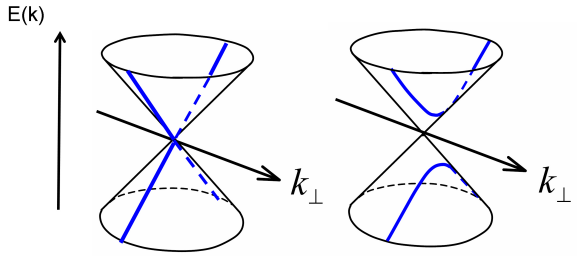

Figure 2.3: Slices (blue) through the graphene band structure. Only the vicinity of one K-point is shown. Depending on the quantization conditions the allowed values of $k_\perp$ can pass exactly through the K-point (left) or not (right). In the first case the nanotube is metallic whereas in the second case a gap opens up between valence and conduction band and thus the tube semiconducts. Adapted from [9].

even at room temperatures. This means in practice that phonon *scattering* is rather suppressed in nanotubes.

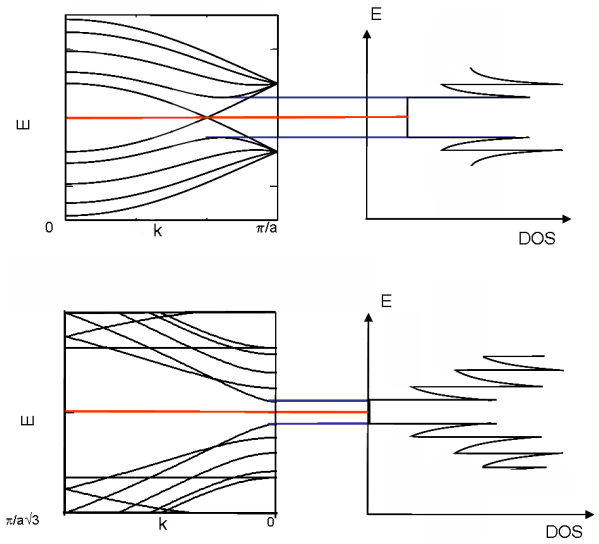

Figure 2.4: Band structure and density of states for metallic and semiconducting nanotubes. Van Hove singularities appear whenever an extra subband is taken into account. Notice the bandgap at E=0 for semiconducting tubes.

Phonon *modes* however are abundant in carbon nanotubes [2]. There exist thus many different ways through which the rolled-up graphene lattice can vibrate. In the *bending mode* for instance, where the tubes' edges vibrate perpendicular to its axis, the phonon spectrum can be of the order of 0.1 - 10 μeV. In the so-called *Z-breathing mode*, the tube vibrates parallel to its axis with phonon energies of the order of 60 - 600 μeV. These two modes mentioned this

far are length dependent and operate at very small energy scales. The other two modes, the *squashing mode* and *radial breathing* mode, lie in energy ranges of 2 to 4 meV and 18 to 25 meV respectively [10]. These energy scales are then more accessible experimentally.

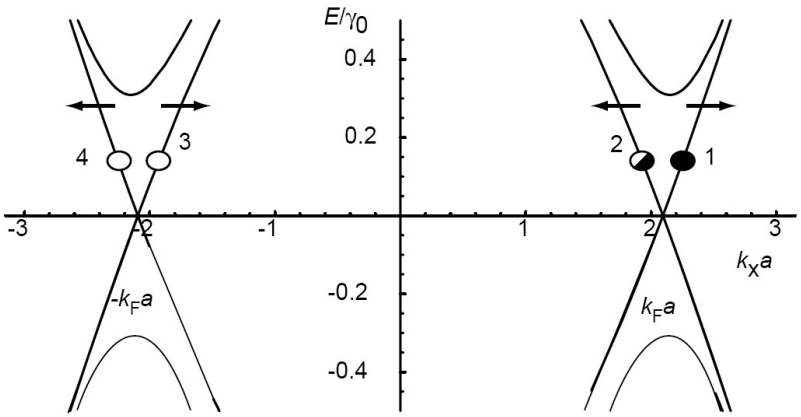

Figure 2.5: Scattering possibilities between two different K-points for an electron starting in position 1 in a metallic nanotube. Only transitions to state 2 are possible through phonon emission. All other transitions are fundamentally not allowed. Adapted from [11].

Chapter 3

Quantum Dots

A quantum dot is a small box that can be filled with electrons (or holes). The name "dot" simply suggests an exceedingly small region in space. Quantum mechanics then postulates that particles trapped in such a region can exhibit discrete, particle-in-a-box types of states. These are *zero dimensional* energy states on which extra electrons can be placed. Normally, even a quantum dot is made out of roughly a million atoms with an equivalent number of electrons. For semiconducting dots virtually all electrons are bound to the nuclei, but there is a small number that are free. These electrons occupy aforementioned discrete 0-D energy states. Since a quantum dot is a generic term for such systems, quantum dots of many different sizes and materials exist: from Stranski-Krastanow self assembled quantum dots to carbon nanotubes. The focus of this thesis is on the latter.

3.1 Single Quantum Dots

All electron transfers on a quantum dot take place through tunneling events. The quantum dot is usually tunnel coupled to two electrodes, the *source* and *drain*, through which particle exchange with the reservoirs takes place. The dot is also capacitatively coupled to a nearby *gate* electrode. There is no tunneling of electrons from gate to dot: the gate is only there to act as an extra experimental knob. By applying a voltage to it, the gate can affect the electrostatic potential of the dot itself.

The properties of quantum dots are dominated by two effects. The first one concerns the Coulomb repulsion between the electrons already on the dot. Any electrons already on the dot cause field lines that make it energetically costly for extra electrons to tunnel on to the dot. An extra electron changes the dot electrostatic potential by $E_C = e^2/\mathrm{C}$, where C is the total capacitance of the dot. Due to this *charging energy*, tunneling of extra electrons can be dramatically suppressed, particularly at low temperatures, since then electrons cannot gain enough energy from thermal fluctuations alone to overcome the charging energy and enter the dot. This phenomenon is called *Coulomb Blockade*.

The second effect concerns electrons on the dot: these are confined in all three dimensions. This leads to the formation of a discrete energy spectrum for electrons, much like the ones displayed by atoms. For these reason QDs are some

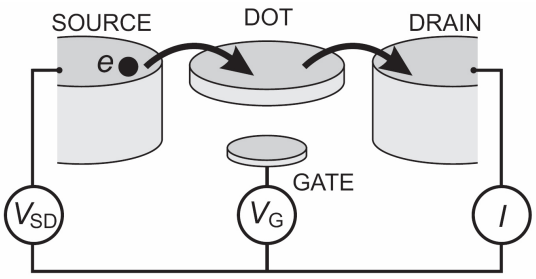

Figure 3.1: A schematic representation of a quantum dot coupled capacitatively to source, drain and a nearby gate. Particle exchange occurs only with the leads.

times referred to as *artificial atoms*. The "particle-in-a-box" energy separation for nanotubes is $\Delta E = \frac{hv_F}{2L}$ [5]. The Fermi velocity is estimated theoretically for nanotubes to be roughly $v_F = 10^6$ ms^{-1} [5]. Therefore even a nanotube of length L of a few μm will show a considerable energy splitting of the order of meV. The advantage of working with quantum dots is precisely that one can connect them to leads and perform electrical spectroscopy rather than optical, as is usually the case for atoms.

For electrons to remain localized on one dot the tunnel barriers have to be sufficiently opaque and the temperature lower than the charging energy as mentioned above. Summing it up

$$R_t >> h/e^2 \tag{3.1}$$

$$e^2/C >> kT \tag{3.2}$$

The first criterion can be met by weakly coupling the dot to source and drain while the second by making the dot smaller or lowering the temperature.

For a more mathematical description of QDs the *Constant Interaction Model* (CI) is usually used. Here one compacts all coulomb interactions of electrons in the dot, and those in the environment by a single, constant capacitance C which is the sum of capacitances between the dot and source, C_S, the drain, C_D, and gate C_G. One also assumes that the single particle energy level spectrum is independent of the number of electrons on the dot. Under these assumptions the total energy U(N) of a dot with N electrons in it and V_S, V_D, V_G the respective voltages on source, drain and gate can be written as:

$$U(N) = \frac{[-|e|(N - N_0) + C_S V_S + C_D V_D + C_G V_G]^2}{2C} + \sum_{n=0}^{N} E_n(B) \tag{3.3}$$

with N_0 the electron charge compensating for positive background charge from the nuclei. The terms C_S, V_S $C_D V_D$ and $C_G V_G$ can be changed continuously. One can think of $C_G V_G$ as the potential the dot would in some sense "like" to have while the last term is a sum over single particle energy levels.

The lowest energy required to add/extract the Nth particle (electron) from a system (dot) is by definition the electrochemical potential μ(N), defined as

$$\mu(N) \equiv U(N) - U(N-1) = (N - N_0 - \frac{1}{2})E_C - \frac{E_C}{e}(C_S V_{SD} + C_G V_G) + E_N \tag{3.4}$$

The first part is the electrostatic energy that has to be paid, while the second part is the chemical contribution that corresponds to putting the particle in a particular state. The electrochemical potentials of *transitions* between *successive ground states* are spaced by

$$E_{add}(N) = \mu(N+1) - \mu(N) = E_C + \Delta E \tag{3.5}$$

This also consists of an electrostatic first part plus the spacing between two adjacent discrete quantum levels ΔE.

For small source-drain voltages, the so called *low bias regime*, electron transport from source to drain is only possible through the dot if a level corresponding to a *transition* between successive ground states is situated inside the *transport window*. If not, the dot is said to be in Coulomb Blockade. To move an electrochemical potential into the bias window one typically uses the gate. By application of voltages one shifts the whole ladder of electrochemical potentials up or down, and can thus bring one level inside the transport window. Electrons can then tunnel *sequentially*, first from source to dot, as they enter the dot makes a transition from the (N-1) to the (N) electron state, and finally off to drain, see Fig. 3.2.

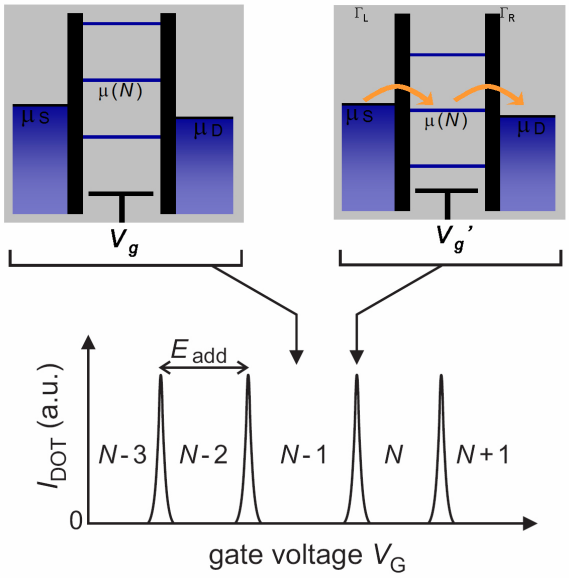

Figure 3.2: Electrochemical potential landscape. Top left: No level is in the transport window (Coulomb Blockade). Top right: by means of the gate one level is brought in the transport window and current flows. Bottom: Current as a function of sweeping the gate voltage. Current peak heights depend on the number of electrons that tunneled during the measurement time and therefore on the tunneling rates to source (Γ_L) and drain (Γ_R). The peak lineshape can be fitted by a Lorentzian. As temperature increases the peaks get thermally broadened.

The second way to lift Coulomb blockade and bring a level in the transport window is by changing V_{SD}. When V_{SD} is increased so much that also a

transition between ground and excited states comes in the bias window electrons through the dot have two paths for tunneling, see Fig. 3.3. This will generally affect the current, the change depending on the tunnel coupling of the two levels involved in these two transitions.

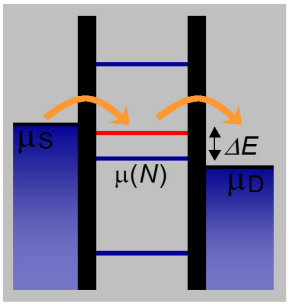

Figure 3.3: Schematic of electrochemical potential landscape in the high-bias regime. The source-drain voltage ΔE is large enough to allow electron transport through two different ways, one of which involves the dot making a transition to an excited state (red).

Finally, by sweeping both gate and source-drain voltage and measuring the dot current one ends up with diagrams where the Coulomb blockade regions appear as diamonds in the V_{SD}-V_G plane. These are the so called *Coulomb Diamonds*, see Fig. 3.4. Where a line for a transition involving one excited state touches the diamond region the bias window exactly equals the energy level spacing. A rule of thumb for the position of the dI/dV_{SD} is that *if a line terminates at the N- electron Coulomb blockade region, the transition necessarily involves an N-electron excited state.*

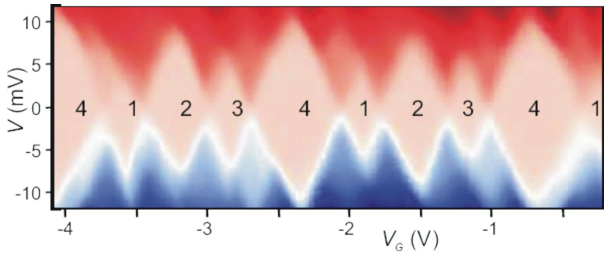

Figure 3.4: Coulomb diamonds diagram for a carbon nanotube. Inside the diamonds no current flows - Coulomb Blockade. The four-fold symmetry denotes the high quality of the nanotube. Reproduced from [12].

3.2 Double Quantum Dots

The next step after single dots is to study systems of more than one dot. Whereas single dots are often described as *artificial atoms*, coupled quantum dots in series (or double dots) can be thought of as *artificial molecules*. Depending on the interdot coupling capacitance, the two dots can form ionic-like (weak

tunnel coupling) or covalent-like (strong tunnel coupling) bonds. Most of the physics behind single dots, like charging and confinement effects are also present here. The mathematical formulation is however slightly different to account for the existence of two dots. Note that the two dots are now coupled: a change in the energy of one dot, for instance through a tunneling event, will affect the energy of the other.

We follow the work of van der Wiel *et al* [13]. At first we treat the quantum dot fully classically. The double quantum dot system can be modeled as a network of resistors and capacitors, see Fig. 3.5. The two quantum dots are

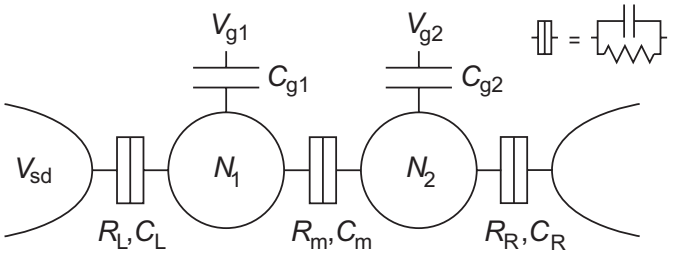

Figure 3.5: A double quantum dot modeled as a network of resistors and capacitances. The dots are represented by the two circles with $N_{1(2)}$ electrons on dot 1(2). The dots are coupled to the leads by a resistor $R_{L(R)}$ and a capacitor $C_{L(R)}$ and to each other by a resistor R_m and a capacitor C_m. Two gate voltages $V_{g1(2)}$ are coupled to the dots through capacitances $C_{g1(2)}$.

represented by the two circles with $N_{1(2)}$ electrons on dot 1(2). Dot 1(2) is coupled to the source (drain) through a capacitance $C_{L(R)}$ and a resistor $R_{L(R)}$ in parallel. The tunnel coupling between the dot is represented by a capacitance C_m and a resistor R_m. Two gate voltages $V_{g1(2)}$ are coupled to the dots through capacitances $C_{g1(2)}$.

$$U(N_1, N_2) = \frac{1}{2}N_1^2 E_{C1} + \frac{1}{2}N_2^2 E_{C2} + N_1 N_2 E_{Cm} + f(V_{g1}, V_{g2}) \tag{3.6}$$

$$f(V_{g1}, V_{g2}) = \frac{1}{e}\{C_{g1}V_{g1}(N_1 E_{C1} + N_2 E_{Cm}) + C_{g2}V_{g2}(N_1 E_{Cm} + N_2 E_{C2})\} \tag{3.7}$$

where $E_{C1(2)}$ is the charging energy of the single dot 1(2) and E_{Cm} is the electrostatic coupling energy. The coupling energy E_{Cm} is the change in energy on one dot when an electron is added to the other dot. These energies can be expressed in terms of capacitances in the network as

$$\begin{aligned} E_{C1} &= \frac{e^2}{C_1}\left(\frac{1}{1-\frac{C_m^2}{C_1 C_2}}\right) \\ E_{C2} &= \frac{e^2}{C_2}\left(\frac{1}{1-\frac{C_m^2}{C_1 C_2}}\right) \\ E_{Cm} &= \frac{e^2}{C_m}\left(\frac{1}{\frac{C_1 C_2}{C_m^2}-1}\right) \end{aligned} \tag{3.8}$$

The electrochemical potential $\mu_{1(2)}(N_1, N_2)$ dot 1(2) is by definition the energy needed to add the $N_{1(2)}$-th electron to dot 1(2), when having $N_{2(1)}$ electrons on dot 2(1). From Eq. 3.6 the electrochemical potentials of the two dots follow as

$$\begin{aligned} \mu_{1,class}(N_1, N_2) &= U(N_1, N_2) - U(N_1 - 1, N_2) \quad (3.9) \\ &= (N_1 - \frac{1}{2})E_{C1} + N_2 E_{Cm} + \frac{1}{e}(C_{g1}V_{g1}E_{C1} + C_{g2}V_{g2}E_{Cm} \\ &\quad + C_L V_L E_{C1} + C_R V_R E_{Cm}) \\ \mu_{2,class}(N_1, N_2) &= U(N_1, N_2) - U(N_1, N_2 - 1) \quad (3.10) \\ &= (N_2 - \frac{1}{2})E_{C2} + N_1 E_{Cm} + \frac{1}{e}(C_{g2}V_{g2}E_{C2} + C_{g1}V_{g1}E_{Cm} \\ &\quad + C_R V_R E_{C2} + C_L V_L E_{Cm}) \end{aligned}$$

Up to now there has been no mentioning of the discreteness of the energy levels in each dot due to confinement of charge carriers. When this discreteness is taken into account, the energy of these states must be added to the electrochemical potential above. The energy to add an electron to the energy level N to dot 1(2) is denoted by $E_{n,1(2)}$ and the electrochemical potential for dot 1(2) can be rewritten as

$$\begin{aligned} \mu_1(N_1, N_2) &= \mu_{1,class} + E_{n,1} \quad (3.11) \\ \mu_2(N_1, N_2) &= \mu_{2,class} + E_{n,2} \end{aligned}$$

The change in $\mu_1(N_1,N_2)$, if at fixed gate voltages N_1 is changed by one, $\mu_1(N_1+1,N_2)$ - $\mu_1(N_1,N_2)$ = E_C+ ΔE is called the *addition energy* of dot (1). The reasoning for dot (2) is exactly the same.

3.2.1 Stability diagram for the linear regime

As in the single dot case, the *linear* regime occurs when the bias voltage is infinitesimally small. From the formulas given in Eq. 3.11 a charge stability diagram can be constructed giving the *equilibrium* numbers of electrons on dot 1(2) as a function of the gate voltages V_{g1} and V_{g2}. We define the electrochemical potentials of the source and the lead to be zero if no bias voltage is applied, μ_L=μ_R=0. The equilibrium charges on the dots are then the largest integer numbers for which $\mu_1(N_1, N_2)$ and $\mu_2(N_1, N_2)$ are both less than zero. If either one is larger than zero electrons can escape through that leads but if either one is less than zero, electrons can tunnel from the leads into the dots and these states become filled. This constraint, as well as the fact that N_1 and N_2 must be integers, produce hexagonal stability diagrams. These are the double dot analogs of the single dot *Coulomb diamonds* diagrams, see Fig. 3.6(a).

A current is measured when an electron can tunnel through the double dot. An electron can tunnel through the dot in two ways. At the points denoted by an (•) in Fig. 3.6(a) electrons tunnel through the states (N_1, N_2), $(N_1 + 1, N_2)$ and $(N_1, N_2 + 1)$. This cycle is known as the electron cycle. Note that three states must align. This happens at the intersection of three lines in the stability diagram. This tunnelling process is schematically shown in Fig. 3.6(b) as the round arrow around the (•). At the point denoted by a (∘) the electron tunnels through the states (N_1, N_2), $(N_1, N_2 - 1)$ and $(N_1 - 1, N_2)$. This can

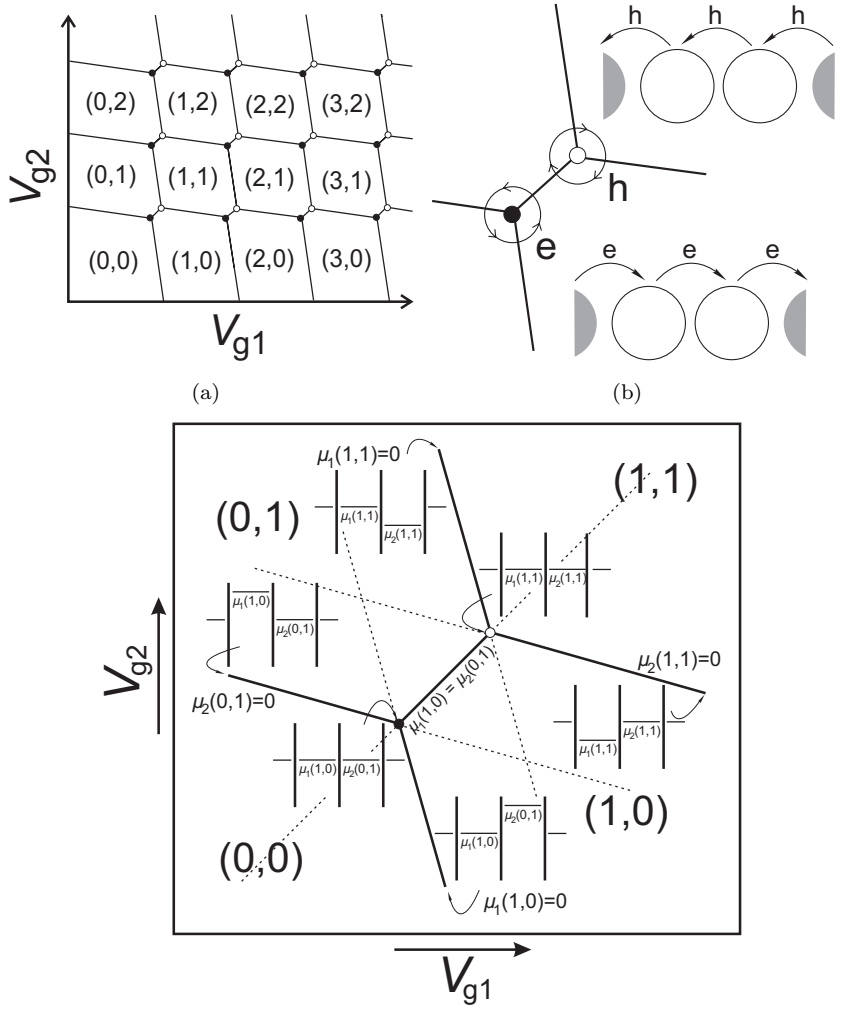

Figure 3.6: Stability diagram for a double dot in the intermediate coupling regime. The stability regions as a function of V_{g1} and V_{g2} are given in (a). Transport through a double dot at the triple points is drawn in (b). At the ($\bullet$) triple point, transport through the double dot happens through the states (N_1, N_2) (N_1+1, N_2) (N_1, N_2+1). This denotes an electron tunneling to the right through the double dot system and is represented by the round arrow around this triple point. At the ($\circ$) triple point, transport happens through the states (N_1, N_2) (N_1, N_2-1) (N_1-1, N_2), so effectively a hole moves through the dot in the opposite direction of the applied bias. Note that to have transport in both of these cases on needs to go *around* the triple points. The configuration of the levels in the double dot is given for several points here. The number of electrons in the left and right dot is given by (N_1, N_2) and values for some of the electrochemical potential are given.

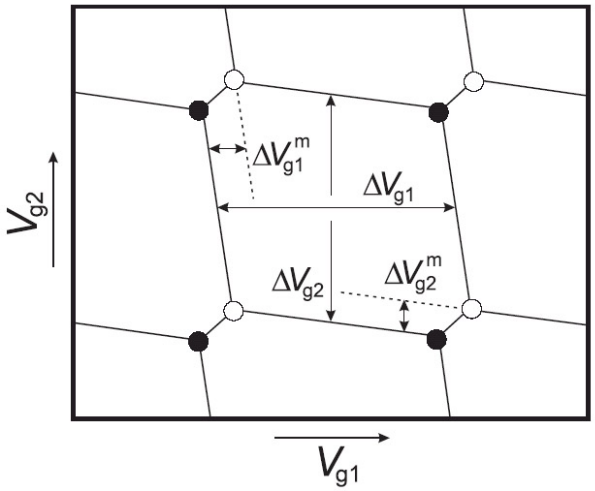

Figure 3.7: Schematic stability diagram showing the honeycomb pattern and respresentative Coulomb peak spacings.

be interpreted as the sequential tunneling of a hole in the direction opposite to the electron. This cycle is illustrated as the round arrow around the (∘).

The gate capacitances of the system can be directly related to the dimensions of the honeycomb cells through

$$\Delta V_{g1(2)} = \frac{e}{C_{g1(2)}} + \Delta E \tag{3.12}$$

Finally, from the relation Eq. 3.13 the capacitative coupling C_m between the two dots can be calculated through

$$\Delta V_{g1(2)}^{m} = \Delta V_{g1(2)} \frac{C_m}{C_{1(2)}} \tag{3.13}$$

3.2.2 Large bias regime

If the bias is increased further, two things happen. First, the chemical potentials of the left and right dot are affected because the voltages on the left and right dot are coupled to the chemical potentials as given in Eq. 3.9. Secondly, the conductance regions change from triple points in the linear regime to triangular shaped regions in this large bias regime (see Fig. 3.8). The dimensions of the triangles δV_{g1} and δV_{g2} are related to the applied voltage as

$$\alpha_{1(2)} \delta V_{g1(2)} = \frac{C_{g1(2)}}{C_{1,(2)}} e \delta V_{g1(2)} = |eV| \tag{3.14}$$

where α_1 and α_2 are voltage-to-energy conversion factors. Note that resonant transport occurs only through the base of the triangle where ground states for the two dots are aligned. However, *inelastic tunneling* and *co-tunneling* can contribute to a finite current *inside* and *outside* the triangles.

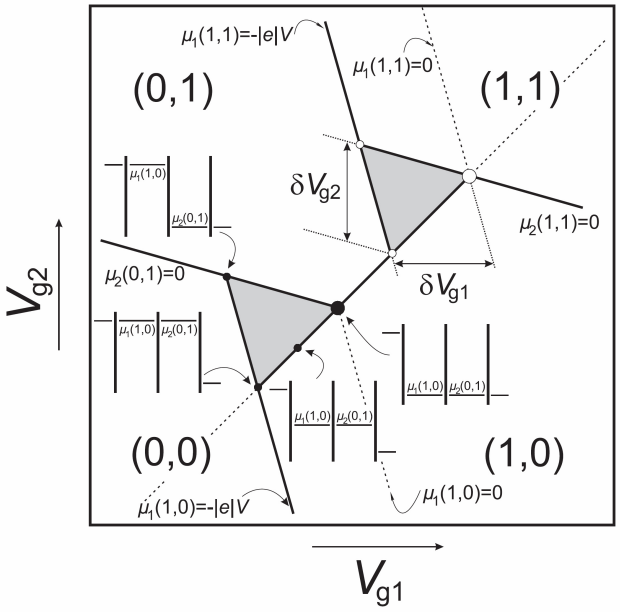

Figure 3.8: Large bias triangles for a double quantum dot. Current is possible in the area inside the triangle. The conditions $\mu_L = -|e|V \geq \mu_1$, $\mu_1 \geq \mu_2$ and $\mu_2 \geq \mu_R = 0$ determine the boundary of these large bias triangles. The configuration of the levels in the dot is given for several points in this diagram. The number of electrons in the left and right dot is given by (N_1, N_2). Configurations for some electrochemical potentials are also given for some positions.

3.2.3 Excited states

For even larger bias it happens that, like in single dots, excited states can also contribute to transport through the double dot system. The transport window is now large enough to accommodate more than a few transition probabilities, and some of them can involve excited states of the left and/or right dot. Electrons can now tunnel in and out through these states and therefore more channels for tunneling exist. This will lead to a change in current.

To understand how excited states fit in the triangle picture described this far it is instructive to refer to the toy example of Fig. 3.9, adapted from Wouter Naber [14]. For simplicity we only consider one excited state (ES) in the left and one in the right dot. We also assume the excited state of the right dot lies closer to the right dot ground state (GS) than the left dot's ES does to its respective GS. These excited states can be due to phonons or spin for instance. In the lower left corner of the triangle both GSs are aligned and in resonance with the right lead. If one moves over the basis of the triangle, from left to right, the GSs remain aligned but shift equally down in energy. Thus, at the bottom right corner of the triangle the ground states are still aligned but now are in resonance with the left lead chemical potential. This is why throughout the basis of the triangle a strong current is observed which corresponds to ground state transport as mentioned earlier.At some point while moving through the

basis of the triangle the excited states come in the transport window. Only the onset of the right dot ES signifies a change in current (green part in Fig 3.9) since an electron now has two ways to transverse the dot. The left excited state always lies higher than the right dot's GS and ES and is therefore inaccessible.

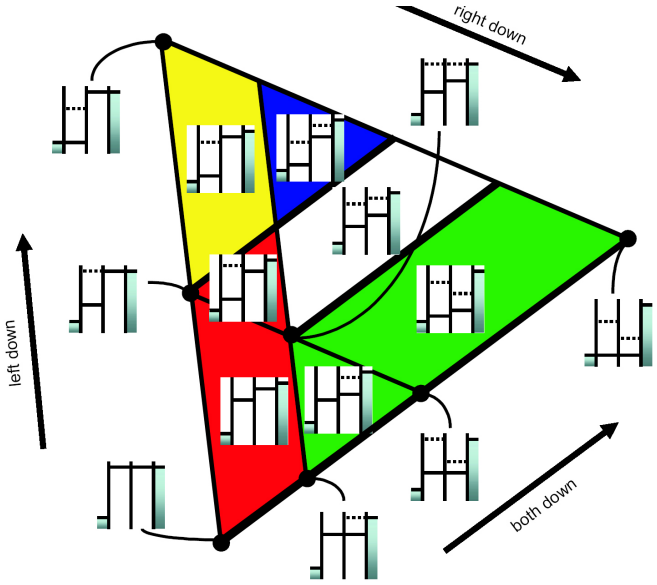

Figure 3.9: Schematic of several areas inside a large bias triangle for negative bias and one excited state in every dot. Different colors denote change in current. The relative positions of electrochemical potentials in the left and right dot are also given for some places. Adapted from [14].

This argumentation holds for any line parallel to the base of the triangle. Therefore, there exists a line parallel to the left side of the triangle for which the current increases if we move from the left to the right side. If one starts from the bottom left corner but moves over the left side of the triangle the right dot ground state is kept aligned with the left lead and the states in the left dot moves down. At some point the left dot ES enters the bias window. At this point the left dot ground state is aligned with the right dot excited state and so the current is resonant. For this reason the current increases again (onset of yellow region). When we cross this point, an electron in the right dot now has two possibilities to tunnel into the left dot. A similar argumentation can be given for any line starting from the basis of the triangle parallel to the left side of the triangle. If the bias becomes even larger the two triangles start to overlap. For one ES in the left and one in the right dot, a schematic diagram is given in Fig. 3.10(a).

If one plots a current lineshape trace inside a triangle as a function of the energy separation ϵ of the left dot GS and the right dot GS, then at $\epsilon = 0$ the two GSs are aligned and transport is resonant. The electron entering the right dot only carries information about the lorentzian broadening of the left dot's level and has lost all information on the Fermi-Dirac thermal broadening of the reservoirs where it originated from. Effectively, the first dot acts as a

low-temperature pass filter for the second dot. Hence, for resonant tunneling, the lineshape obtained is a lorentzian given by [13] as

$$I(\Delta E) = e\frac{\Gamma_3|t_{12}|^2}{(\Delta E/h)^2 + \frac{\Gamma_3^2}{4} + |t_{12}|^2(2 + \frac{\Gamma_3}{\Gamma 1})} \tag{3.15}$$

where $\Gamma_{1,3}$ are the tunneling rates through the left and right leads respectively, ΔE the difference in energy between two discrete energy levels in the two dots and $|t_{12}|$ is the tunnel rate between them. In this way one can measure the *intrinsic lifetime* of states in the two dots without interference of thermal broadening from the reservoirs.

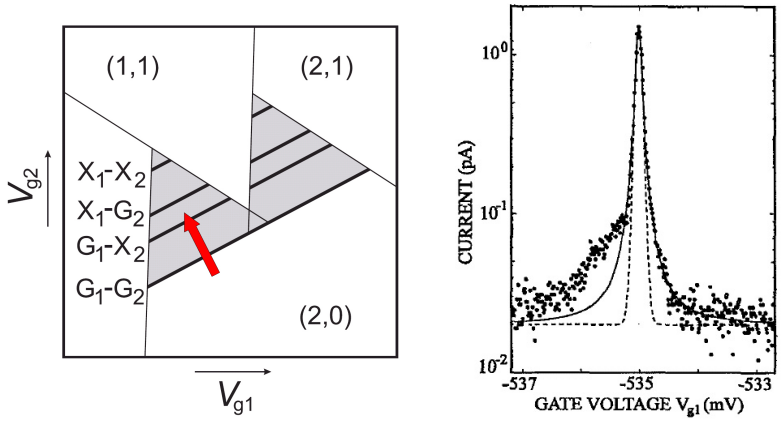

(a) (b)

Figure 3.10: a) Schematic stability diagram for very large bias. The black lines correspond to transport through different combinations of ground and excited states between the two dots. The red line corresponds to a cut through the triangle where the current lineshape is measured (see Fig. 3.10(b)). Adapted from [13]. b) Current lineshape close to $\epsilon = 0$. Data points are fitted to a Lorenzian. Reproduced from [15].

Any coupled quantum dot can be approximately modeled as a two-level system. Here only one level in each dot is of significance, as for instance two ground states. Transport through the system can then occur in two ways: when the GSs are aligned (resonant tunneling) the current is elastic as no energy is dissipated. When the two levels are misaligned there has to be some sort of medium that offers/receives the energy mismatch between the electrochemical potentials of the two dots. This medium could be for example photons (*Photon Assisted Tunneling*) or phonons. In large bias triangles like the ones in Fig. 3.10(a) the elastic current peaks at $\epsilon = 0$ at the base of the triangle where the ground states are aligned, while finite current inside the triangles belongs to inelastic tunneling events. Theory predicts [16] that inelastic tunneling for a two level system such as a double dot coupled to a bosonic environment has a $|t_{12}|^2$ dependency. Excited states spectroscopy can therefore also be performed by tuning the middle barrier between two coupled dots to higher values.

Chapter 4

Single Electron Transistors

A single-electron transistor (SET) is a three terminal device. It consists of a metallic island that is tunnel-coupled to source and drain electrodes, and capacitatively coupled to a nearby gate that tunes it's electrostatic potential. SETs have been shown to function as ultra sensitive electrometers, being able to sense even fractions of an electron charge. It can therefore be used when current transport measurements become too difficult, as for instance if the current is too small to measure. One then typically exchanges current measurement for charge measurement. It is this characteristic of an SET that makes it an ideal candidate, along with *quantum point contacts* (QPCs) for measuring charge transport through nanotube quantum dots.

4.1 SET Fabrication

Single Electron Transistors are usually fabricated using the so-called *double-angle* (or *shadow*) evaporation technique. One starts with an SET pattern

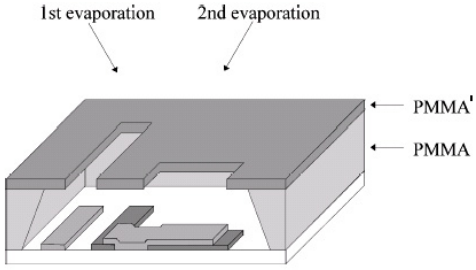

Figure 4.1: Fabrication of an SET using the standard double angle evaporation technique. The sample is first evaporated under one angle (dark), then oxidized, and finally evaporated under the opposite angle (light). A tunnel barrier is formed at the overlap area. Notice the bridge structure formed by the PMMA. Without it the two layers would overlap everywhere and no small tunnel junction would be possible. In this image only the evaporation under one of the SET bridges is visible. Adapted from [17].

already written and developed on the resist. The first step involves a metal

evaporation under an angle from the vertical. This angled evaporation results in a shifted pattern on the Si wafer. In order for this shift to take place, a sufficient resist undercut should exist. In the second step, the surface of the first metallic layer evaporated previously is oxidized. In our case, where Al is the metal of choice, this will result in a thin Al_2O_3 layer being formed. Finally, the sample is re-evaporated under an angle opposite to the one used in the first step so that the pattern is now shifted in the opposite direction.

With a proper choice of evaporation angles in the first and third steps one can achieve a very small overlap area between the two metal layers, see Fig. 4.1. At this small area, the tunnel junction, a metal-insulator-metal interface is formed. Effectively, electrons have to tunnel through the oxide to move from

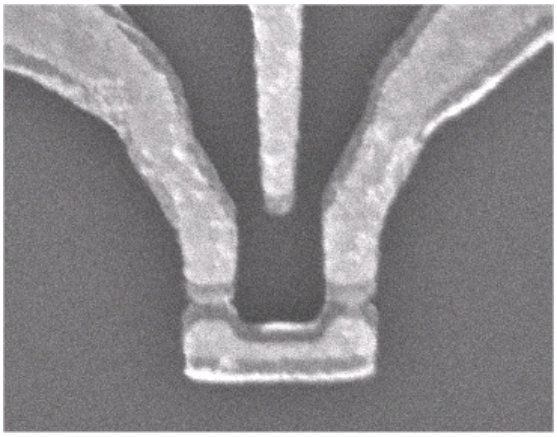

Figure 4.2: SEM image of the SET design used in this work. The island is capacitatively coupled to a nearby gate and connected through tunnel barriers to source and drain. Compare to Fig. 4.1.

one metal layer to the other. Aluminum is usually the metal of choice for in this case since the oxide it forms grows very uniformly, without creating structural defects that could function as pinholes through which electrons would be able to move through the oxide layer.

The junction overlap is what sets the capacitance C of the junction. The charging energy $E = \frac{e^2}{2C}$ is in turn set by the overlap area. Finally, the resistance R of the junction is set by the oxidation time, this dependence not generally being a linear one [17]. The tunnel junction area is set by a combination of factors: evaporation angle, resist bridge thickness and resist height. For larger angles the junction overlap becomes larger. If the bridge width is for example too large, larger evaporation angles are also needed to achieve overlap. Finally, a larger resist thicknesses require smaller evaporation angles to achieve the same overlap as with smaller resist thicknesses.

4.2 SET Characteristics

As mentioned above the SET is a three terminal device where a metallic island is connected through tunnel barriers to source and drain electrodes and coupled capacitatively to a nearby gate. An SET therefore resembles a Field

- Effect Transistor (FET) is the sense that both are three-terminal devices. However, the FET channel is replaced in the SET by the metallic island and the tunnel barriers. This is a crucial difference as in SETs electrons tunnel in a correlated manner (sequentially) and do not move in unison as is the case for FETs.

The description above is very much reminiscent of a quantum dot, as discussed in chapter 3.1. The difference is that for SETs the island is always metallic while for QDs it can also be semiconducting. In this respect the characteristics of an SET very much resemble those of a quantum dot: the familiar coulomb peaks when sweeping the gate voltage and the Coulomb diamonds in the V_{SD} - V_G plane are also present.

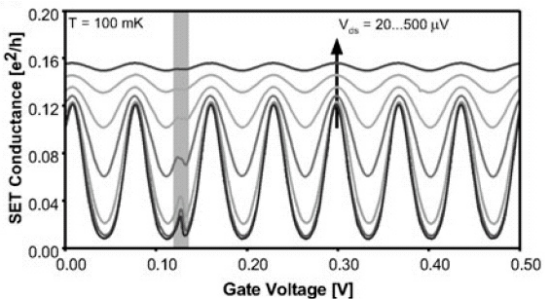

Figure 4.3: Conductance of an SET as a function of gate voltage. The familiar coulomb peaks are visible. Low to high corresponds to higher bias voltages. Note that the peaks are now equally spaced. The grey area corresponds to switching: some defect in the vicinity of the SET electrostatically de-tunes the effective voltage from the gate and thus the SET current also changes. Reproduced from [18].

Since the energy level spacing δ is much smaller in SETs due to the large island size it makes little sense to talk about zero-dimensional states here. The Coulomb diamond diagram is therefore modified as shown below when sweeping also V_g: Inside the black areas Coulomb Blockade dominates and the electron number in the island stays fixed. Just above and below the blockaded regions the electron number can change by one. This is where single electron tunneling can take place. If one moves even further away from $V_{SD} = 0$ the electron number can change by two: tunneling can occur twice.

The slopes of the diamonds provide information on the left and right tunnel barrier capacitances. Unequal tunnel capacitances will yield skewed coulomb diamonds. The left diamond slope is equal to -C_G/C_L while the right diamond slope is given as $C_G/(C_R + C_G)$. The diamond skewness is proportional to the difference (C_L-C_R). Since the capacitance of each junction is defined in our case by the overlap area A formed between two consecutive angled metal evaporations, the so called *double angle evaporation technique* [see section 4.1], one can extract information about the quality of evaporation and the bridge resist profile. A difference in left and right tunnel resistances generally results in skewed Coulomb diamonds. However, a difference in resistance between the two tunnel junctions will result in skewed Coulomb peaks.

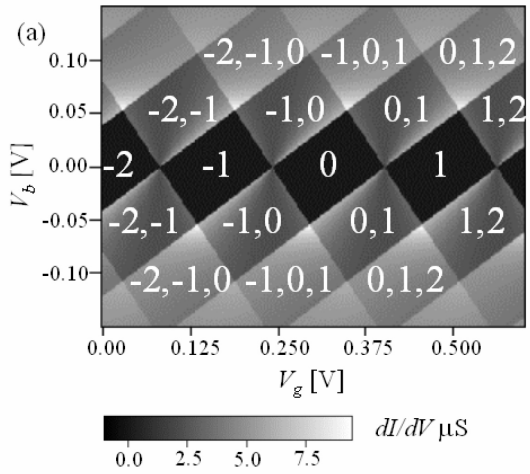

Figure 4.4: Differential conductance calculated for an SET as a function of the gate voltage and the bias voltage. The charge states at low kT are noted. Reproduced from [19].

4.3 SETs as Charge Detectors

It becomes evident from Fig. 4.3 that the voltage or equally *the charge* on the SET gate controls in a very sensitive way the source-drain current. This concept lies at the heart of the idea of using an SET as a very sensitive charge electrometer: a small change in the charge of the gate can affect the measured conductance.

Since the SET is in reality not only coupled to its own gate but to the whole environment, a nearby quantum dot also electrostatically affects the island so that it can be thought of as an effective second gate. When a single electron tunnels in or out of the dot the dot's potential changes. This will in turn affect the SET by shifting the whole $V_{g,SET}$ by $\alpha\delta V_{g,dot}$, where α denotes the coupling of the dot to the SET and δV_{dot} is the change in the dot potential due to the tunneling event. If for instance the SET is normally biased at some $V_{g0,SET}$ value corresponding to a Coulomb valley, the *new* voltage $V_{g0,SET}+\alpha\delta V_{dot}$ biasing the SET could be shifted enough to produce a Coulomb peak. This is the concept underlying the usage of the macroscopic SET for charge sensing on structures much smaller than the SET itself, such as a quantum dot, and for charges too small to measure, such as a single electron. This charge sensitivity has been shown to be as high as $10^{-5}e/\sqrt{Hz}$, very close to the theoretical limit of $10^{-6}e/\sqrt{Hz}$ [20]. This means that one could detect a charge variation of 10^{-5} electrons in a one-second measurement, and the sensitivity increases with the square root of the measurement time.

In practice it is convenient to bias the SET so that its conductance G corresponds to halfway up a Coulomb peak. There, the SET conductance slope is the highest and therefore even a small change in $V_{g,SET}$ affects the conductance significantly. However, to induce tunneling events on the quantum dot in the first place the dot's plunger gate also needs to be varied. Since this is also cou-

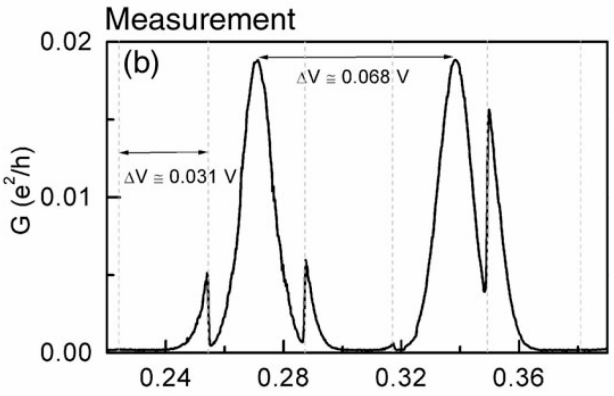

Figure 4.5: SET conductance measured as a function of one of the side gate voltages of a double dot configuration. Large period oscillations correspond to charging of the SET island. Small superimposed oscillations correspond to charge transfer in the double dot system. Note that the conductance changes the most halfway up the Coulomb peak. The SET plunger gate is on ground. Reproduced from [18].

pled to the SET, a voltage on the dot plunger gate will de-tune the SET from the voltage setpoint mentioned above. To *compensate*, one applies a voltage

$$V_{g,SET} = V_{g0,SET} - \alpha V_{plunger,dot} \tag{4.1}$$

Then, the charge induced by the dot plunger gate is compensated by the SET side gate: the SET now only senses the remaining part of the dot voltage, V_{dot}. This is depicted in Fig. 4.6.

The SET voltage consists of two contributions. The first is a linear part due to the linear increase of voltage of the Carbon Nanotube side gates that is required to induce tunneling events. The second contribution comes from to the

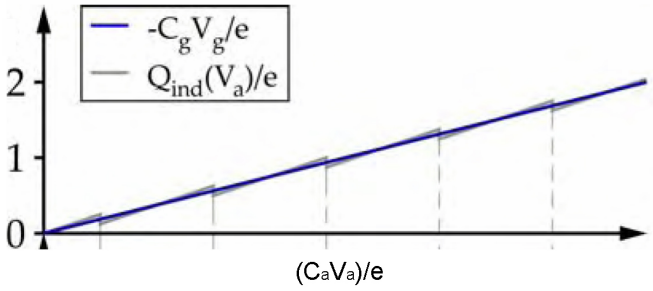

Figure 4.6: Induced charge on the SET island by sweeping the nanotube side gate. The blue trace corresponds to a linear increase in island voltage due to the linear increase of the nanotube side gate. Dot tunneling events, marked out with dashed lines, produce changes in the dot's voltage in a sawtooth like manner. This second contribution is superimposed (grey) on linear term mentioned above. Through compensation the linear term can be canceled out. Adapted from [21].

sudden change of the dot potential when tunneling events take place (dashed lines)which has a sawtooth character. In compensation the linear increase in the voltage sensed by the SET due to the dot side gates (blue in Fig. 4.6) is effectively canceled out and only the sawtooth contribution from tunneling events remains.

By comparing Fig. 4.1 and Fig. 4.5 it is easy to see that background charge noise in the vicinity of the SET gives a signal similar to that of an electron transfer in a close-by quantum dot. These two signals can be confusing, producing an SET conductance trace where it is difficult to interpret what event causes the changes in conductance. To circumvent this problem a second SET can be fabricated in the vicinity of the first. By correlating the signal coming from the first to the signal coming from the second SET it is possible to more accurately determine which processes belong to the dot and which belong to electrostatic background noise. Particularly for double quantum dot architectures where one electron exits the left dot and enters the right, the first SET is coupled more to the left dot (and thus mainly senses the "exit" event in the left dot) while the second SET is coupled more to the right dot (and thus mainly senses the "entrance" event in the right dot). By correlating the two signals any background noise could be filtered out.

Chapter 5

Fabrication

The fabrication time to make a working carbon nanotube quantum dot sample is about two weeks. During this time there is a great number of steps involved in the process and this makes the fabrication line quite detailed. The more complicated the structure gets, for instance by making double dots or fabricating SETs, the more difficult fabrication becomes. Since the majority of the project was spent inside the cleanroom fabricating samples, it is worthwhile to give a detailed description of the fabrication process as well as some examples of problems commonly encountered. All fabrication was done in the Delft Institute for Microelectronics and Submicron Technology (DIMES).

5.1 Fabrication of Carbon Nanotubes

One typically starts out with an ordinary silicon wafer $19x19$ mm wide. The bottom side of the wafer is heavily doped and can act as a supplementary back gate while the top wafer part is oxidized to insulate the structures on the surface from the back gate.

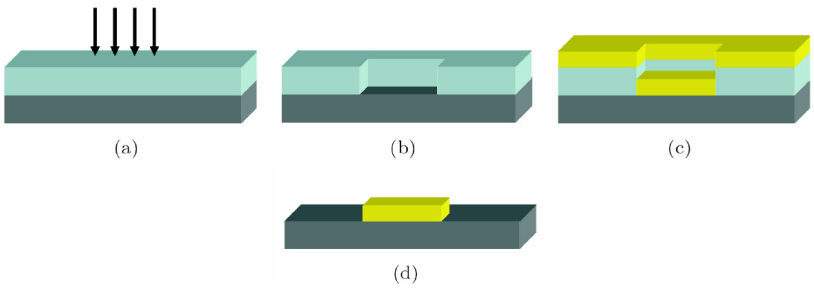

Figure 5.1: Schematic of the fabrication cycle: a) the resist (light blue) is spinned on the wafer (grey) and exposed to electrons, b) exposed part is removed during development, (c) metal (yellow) is evaporated on the entire wafer, and d) unwanted metal is lifted off through an acetone bath. Adapted from [14].

After an initial procedure of cleaning the wafer in a series of baths through acetone, fumic nitric acid, water and isopropylique alcohol (IPA), the first two levels of resist are spinned. In our case the PMMAs used in all fabrication steps

where PMMA 350K 3% in chlorobenzene while the second layer is PMMA 950K 2% in chlorobenzene. The two resist thicknesses are chosen for most devices to be exactly 150 and 100 nm respectively. The top resist layer is most sensitive to electron irradiation and therefore functions as a mask for the bottom layer and in parallel helps achieve a good undercut of approximately 60 nm from each side.

After the resist is spinned and baked, the pattern to be written is designed with the help of DesignCAD and exported through CATS. The wafer is then exposed to electrons inside a Leica EBPG 5K Plus, see Fig. 5.1a, where the pattern is written. Afterwards the wafer is developed for 2.5 minutes in MIBK:IPA (1:3) and 1 minute in IPA. The development process removes the exposed part of the resist so the end result is a wafer with certain parts covered by 250 nm of resist while others are completely stripped of it, see Fig. 5.1b. Metal is then evaporated on the whole wafer under UHV conditions, Fig. 5.1c. The last step is lift-off: the metal-covered wafer is placed in warm acetone for as much time as required to remove the remaining resist and metal from unwanted locations, see Fig. 5.1d.

The procedure described above is repeated in four cycles for every sample we make. The first cycle involves the fabrication of 75 nm high Pt markers with a bottom Ti layer of 2 nm to achieve good adhesion to the SiO_2. Some of the markers serve as optical markers, guiding the eye, other serve as AFM markers (for locating nanotubes later), while the rest are EBPG markers that help the EBPG align the sample prior to writing on it.

The second cycle involves depositing a catalyst solution onto the wafer in predefined positions. Using a Chemical Vapor Deposition method carbon nanotubes grow randomly from these positions. The catalyst is made out of 40 mg of $(Fe(NO)_3)_3 9H_2O$, 2 mg $MoO_2(acac)_2$(Sigma Aldrich) and 30 mg of Alumina nanoparticles (Degussa Aluminum Oxide C) mixed in 30 ml of methanol and sonicated for 1 hour. After covering the entire wafer with catalyst the sample is placed in a furnace for 5 minutes at a temperature of 150 ^{o}C. To allow catalyst only at predefined positions liftoff then takes place. Finally, the wafer is placed in a quartz tube, heated to 900 ^{o}C and a series of combinations of argon, methane and hydrogen flows are passed over the wafer.

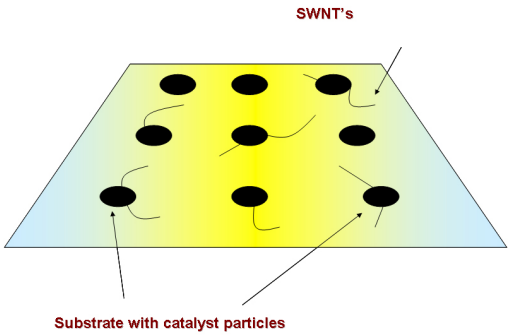

Figure 5.2: Schematic of a silicon wafer with catalyst particles at predefined position. Nanotubes grow out of the catalyst particles randomly.

In the third cycle Atomic Force Microscopy is used (see Fig. 1.1) to locate

the nanotubes on the sample based on their position relative to the predefined AFM markers from step 1. A few of them are chosen and Pd contacts are evaporated on them. The Pd contacts act as source and drain electrodes that can pass current through the tube. Palladium is the chose here because of the very good contact it makes to semiconducting nanotubes, such that Schottky barriers are avoided at the interface of Pd and nanotube. After the Pd contacts are written and evaporated, probe stationing at room temperature takes place. Those nanotubes that show the lowest resistances, of the order of a tens of kΩ, are chosen.

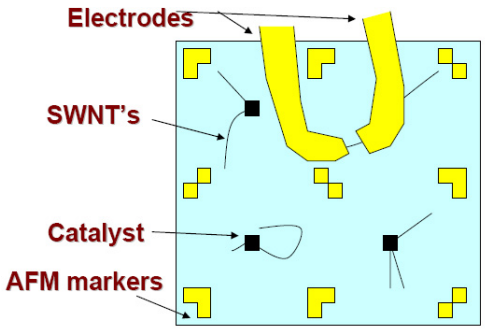

Figure 5.3: Schematic of a silicon wafer with catalyst particles at predefined position. A few nanotubes are chosen and contacted by Palladium source and drain electrodes for electrical measurements.

In the fourth and last cycle the narrow top and plunger gates are written on the two resist layers mentioned above and later evaporated with Aluminum. The nanotube quantum dot narrow top gates in our samples have a width of about 30 nm and are spaced by approximately 400 nm, thus forming two coupled dots of equal size. The end result looks similar to Fig. 1.2. A point to note is that the SET structures are also written in the fourth cycle, together with the top gates and aluminum contacts. Because this requires a double angle evaporation, as mentioned in the previous chapter, the top gates and SET structures need to be perfectly aligned. Otherwise the two directions of evaporation will cause an unwanted broadening and shifting of the dot's top gate structure or it can happen that the structure will not be at all on the substrate. After a series of tests we determined that the optimum evaporation angles for 150 nm of PMMA 350K 3% in chlorobenzene and 100 nm MMA 950K 2% in chlorobenzene were $\pm 15^o$ with an oxidation time of 10 minutes at 100μbar inside the loadlock. These values yield junction overlaps of about 60 nm reproducible over a wide range of samples.

5.2 Carbon Nanotube Fabrication Issues

The most common problem concerning nanotube fabrication involves primarily problems with liftoff of the catalyst. If liftoff is not successful catalyst particles are scattered everywhere on the wafer and not only in predefined positions, see Fig. 5.4(a). This means that in the next step, the CVD growth, nanotubes will be intertwined on the whole wafer. In principle a different liftoff

procedure, accompanied by sonication can be carried out. However there is a risk that sonication will remove all catalyst from the wafer, even from the predefined positions.

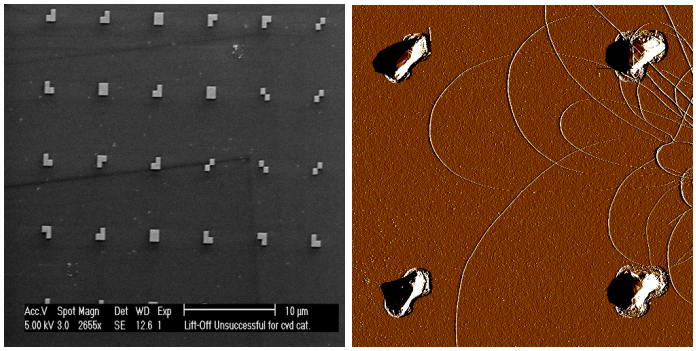

(a) (b)

Figure 5.4: Left: SEM image of the AFM markers on our wafer and catalyst particles. Note that catalyst particles are scattered everywhere and not only in predefined positions. Right: Intertwined nanotubes on a silicon wafer. None of these nanotubes can be singled out to perform electrical measurements as all of them are shorted.

Another common problem involves the stoichiometry and quality of the catalyst itself. Even with optimum stoichiometry of its different components it can happen that the catalyst particles give too much or too few nanotubes, see Fig. 5.4(b). The amount of nanotubes growing out of the catalyst particles depends critically on the amount of $(Fe(NO)_3)_3$ used during catalyst preparation. For our purposes it is best to have only few tubes growing out of the catalyst particles. Otherwise all the tubes are shorted and individual ones are unaccessible.

5.3 SET Fabrication Issues

The SET is the most difficult part of the fabrication line. A series of problems can affect its performance. The most serious problems have to do with bridge formation, see Fig. 5.5(a) and liftoff. The most crucial ingredient for forming the bridges is the resist thickness: we found that a deviation of $\pm$ 10 nm away from the desired total resist thickness of 250 nm results in no bridge formation. Typically these 10 nm difference occur in the second PMMA layer. Concerning the bridge size we have found that not all combinations of bridge widths and lengths will work. After a series of tests the optimum bridge length and width were determined to be 100 and 75 nm respectively. These yield tunnel junctions with an area of approximately 60 nm. For these values we accomplished SET reproducibilities in our final SET test structures of more than 90%. Note that for a single operational SET *two* bridges have to be formed. This requirement makes fabrication even more difficult. The reason for the collapse of the bridges is for the bigger part the overexposure from the electron beam that creates a very big undercut under the bridges, see Fig. 5.6, resist non-uniformity and to

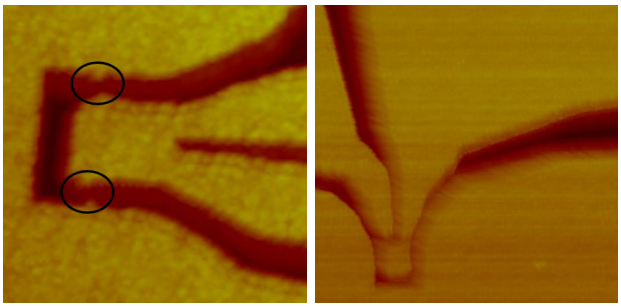

(a) (b)

Figure 5.5: Left: AFM image of the PMMA profile of an SET test structure. The bridge structures are absent on both sides. One can barely detect the positions where the bridges should be (black circles) through local anomalies in the resist profile. Right: AFM image of the PMMA profile of an SET showing the short between gate and source.

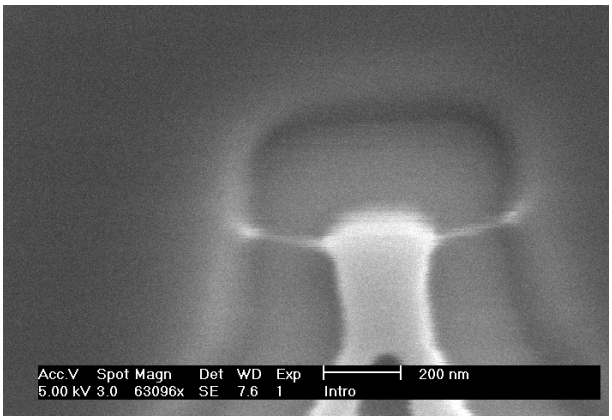

Figure 5.6: SEM image of a test SET structure. Note the fragility of the bridges in the picture. A solution would be to make the bridges wider but this would in turn require a much larger evaporation angle to achieve junction overlap and this can give liftoff problems later.

a lesser part perhaps due to poor handling of the wafer. Concerning the later, we have found that in certain cases the gate of the SET could be shorted to either of the source/drain electrodes, see Fig. 5.5(b). This can occur during the metal liftoff process. It can also occur before any metal is evaporated, as shown in Fig. 5.5. For this reason the gate was moved further away from the island. This resulted in a smaller coupling of our gate to the SET island.

5.4 SET and Double Dot Fabrication Issues

Except for the single nanotubes and SETs, fabrication of double dots either by themselves or together with SETs can also give rise to problems. The most common ones concern either a shifted pattern of gates, for instance top gates

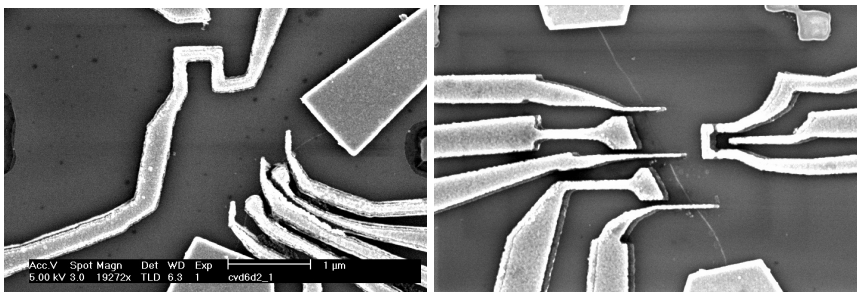

(a) (b)

Figure 5.7: Left: SEM image of a double carbon nanotube system. The gate pattern is so shifted that no dots can be defined. Notice that the SET junctions are also absent, resulting in a short. Right: SEM image of a different carbon nanotube system. Although the gates and SET are properly fabricated, the nanotube has unexpectedly snapped during the fabrication process.

that are so much shifted that they are no longer on top of a tube, see Fig. 5.7(a), or liftoff problems: a dense packaging of structures in a small area can show shorts.

Of crucial importance is the alignment procedure before writing these final structures with the EBPG. Particularly for the SET bridge structures it is important that the height misalignment is not much greater than 5 μm from that of the calibration marker of the holder. A shifted pattern, as well as liftoff problems are visible in Fig. 5.7(b). Finally, it is of interest to note that unexpected problems can also occur as shown in Fig. 5.7(a). Here, one part of the nanotube is cut-off during the fabrication process. To avoid problems of this kind one can generally avoid sonicating during lift-off.

5.5 Measurement Setup

After the fabrication is complete and room temperature measurements have been performed the samples are placed inside a Leiden Cryogenics dilution refrigerator, see Fig. 5.8 and cooled down to mK temperatures. A number of systems such as the cold traps and 1 K-Pot are first used to bring the temperature down to 1 K. Then, a phase transition takes place inside the fridge mixing chamber between two phases of Helium, the liquid phase and the dilute phase, which consumes energy in the form of heat. This phase transition is responsible for bringing the sample temperature even lower to about 30 mK.

All applications of voltages over the sample are performed through digital-to-analog (DAC) converters which are controlled by a home-made computer measurement program. For current measurements through the sample current is first converted to voltage by means of an IV converter and then amplified by an iso-amp.

Figure 5.8: Photo of the measurement setup. On the right side sits the Gas Handling Unit. The refrigerator is situated in the middle, between the Gas Handling Unit and the matrix modules with the DACs at the left edge. All sample currents and voltages, as well as the data storage, is carried out through home-made computer software.

Chapter 6

Measurements

In the first part of this chapter we discuss the characteristics of uncoupled Single Electron Transistors. The results obtained prove our ability to reproducibly fabricate Single Electron Transistors with proper characteristics. In the second part the characteristics of a double carbon nanotube quantum dot are derived. Excited states are visible and a series of experiments are carried out. In the third and final part an attempt is made to use a SET located far away from the dot as a charge detector.

6.1 Uncoupled Single Electron Transistors

We repeatedly fabricated test SET structures to optimize and vary relevant parameters. After a series of tests the optimum parameters for our design were found to be an evaporation angle of $\pm 15^o$, oxidation time of 10 minutes in the loadlock under a pressure of 100μbar and resist thicknesses of 150 and 100 nm respectively for the two PMMA resist layers. The bridge length and

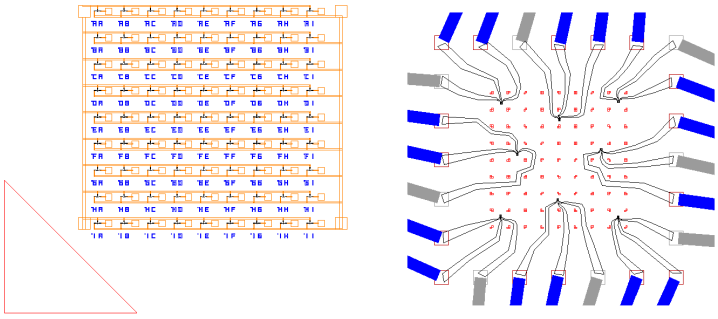

(a) (b)

Figure 6.1: a) DesignCAD image of an SET grid sample. In each column and row the width and length of the SET bridges are varied respectively. b) After determining the optimum dimensions the chosen SET was written on a sample with actual markers to evaluate reproducibility of fabrication under more realistic conditions. Here, eight SETs are connected to thicker contact pads.

width were chosen to be 100 and 75 nm each. After a first rough test on SET grid structures to determine proper width and length ranges, the SETs that showed the most reproducibility were tested on a sample with markers for a better simulation. For samples such as those of Fig. 6.1(b) our reproducibility increased from about 40% to more than 90% during the tests. At room temperature the obtained tunnel junction resistances were reproducibly found to be in the range of 100 to 250 kΩ. We randomly chose and cooled down SETs

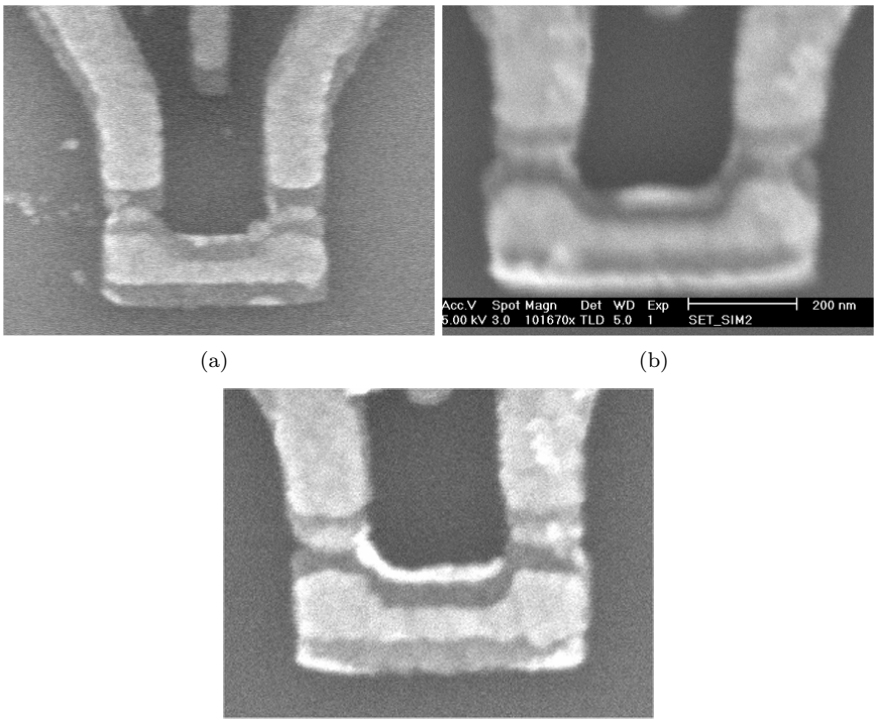

(a) (b)

(c)

Figure 6.2: SEM images of three of SET test structures randomly selected and tested under low-temperature conditions. The tunnel junctions are clearly visible. The tunnel junction area is approximately (120 nm)x(30 nm), in good agreement with our designs. The gate is further away from the structure to avoid liftoff problems.

with junction resistances in the above range. Stability diagrams of differential conductance dI/dV versus bias and gate voltage are obtained for all three of the devices shown in Fig. 6.2. The sharp contrast between Fig. 6.3(a) and a normal Coulomb diamond pattern such as that of Fig. 3.4 is due to superconductivity. Cooper pairs and quasiparticles tunnel through the junctions instead of single electrons. Although the change in the charge of the island is one, three particles have effectively tunneled through the junctions. By comparing Fig. 6.3(a) to literature we extract the value for the superconducting gap for aluminum. For bulk, theory gives $\Delta \approx 0.21$ meV. According to literature [22] the position of the blue arrow in Fig. 6.3(a) corresponds to $(4\Delta/e)$. We then extract a value of approximately 0.19 meV, very close to the theoretical value. It should be noted

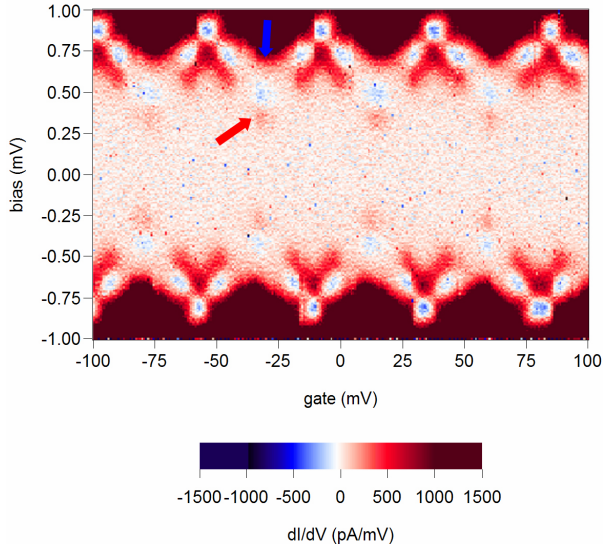

(a)

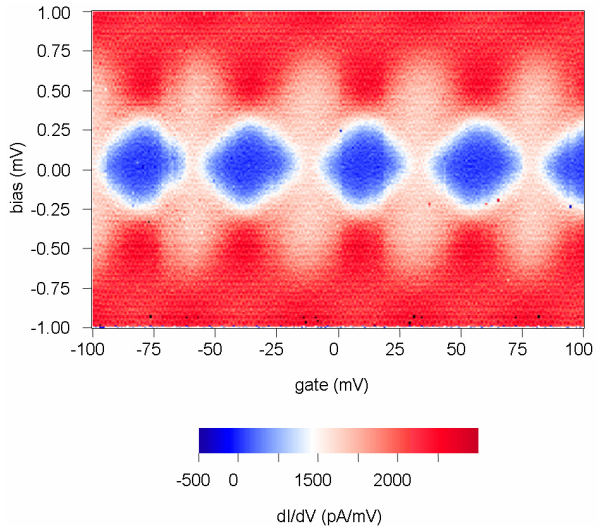

(b)

Figure 6.3: Differential conductance measured for sweeping both SET gate and bias voltages for the sample from Fig. 6.2(a). a) Superconducting Coulomb diamonds. We extract the value of the charging energy (red arrow) and the value of the superconducting gap Δ of Aluminum (blue arrow). b) After application of a magnetic field of B = 1 Tesla superconductivity is destroyed. The difference between (a) and (b) can be attributed to simultaneous tunneling of Cooper pairs and quasiparticles through the junctions [16].

that the value of Δ can fluctuate in thin superconducting aluminum films due to grain formation for instance [23]. By application of a magnetic field B = 1 Tesla superconductivity is destroyed. The charging energy can be directly read

off Fig. 6.3(b) to be $E_C = 0.3$ meV while the conversion factor from voltage to energy, α, is approximately $\alpha = 0.015$. Using the respective formulas (see page 29) we obtain the capacitances as $C_L = 128$ aF, $C_R = 114$ aF and $C_G = 1.1$ aF respectively.

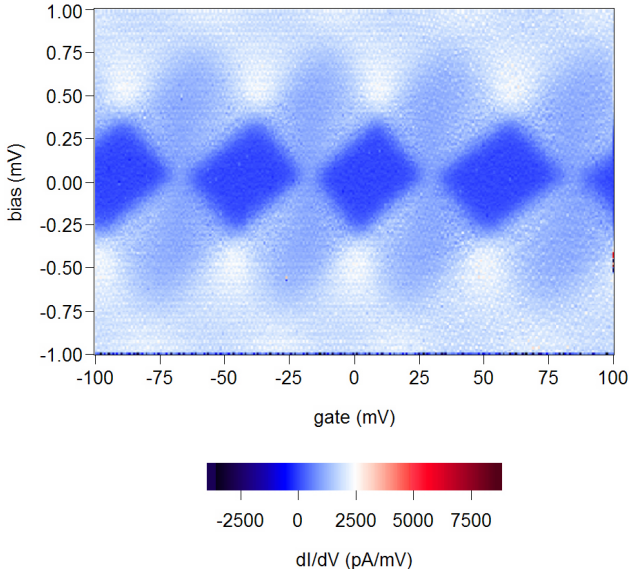

(a)

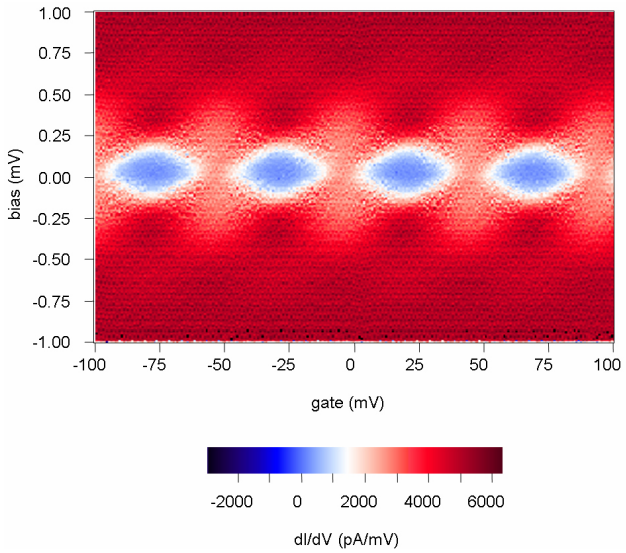

(b)

Figure 6.4: Coulomb diamond plots in the normal state obtained for samples no. 2 and 3. The charging energies are in both cases approximately the same.

Similarly the coulomb diamond plots for samples in Fig. 6.2(b) and Fig. 6.2(c) were extracted. We calculate the capacitances for the sample of Fig. 6.2(b) and find them to be $C_L = 45$ aF, $C_R = 62$ aF and $C_G = 1.15$ aF. The small C_G is

due to the weak coupling of the gate due to its large distance. In some cases as for instance in Fig. 6.4(a) the single, double and triple-electron tunneling areas are visible next to the blockaded regions.

We plot the current as a function of V_G at $V_{SD} = 0$ mV for the device from Fig. 6.2(b). We compare the shape of the Coulomb peaks obtained to theory [24] given by

$$\frac{G}{G_0} = \cosh^{-2} \frac{\delta E}{2.5kT} \tag{6.1}$$

There is a good correspondence between theory and experiment. The sample temperature we extracted was approximately 800 mK, quite higher than T = 37 mK which was the mixing chamber temperature. We attribute the elevated temperature obtained from theory to our junctions' resistance values: Eq. 3.1 should hold in order for Eq. 6.1 to hold. In our case each tunnel junction, whose value is set by the sample oxidation time, has a resistance that is larger, but not significantly, than the resistance quantum R_Q. This produces roughly the same effect that an elevated temperature would have on the sample, namely tunnel-broadened peaks.

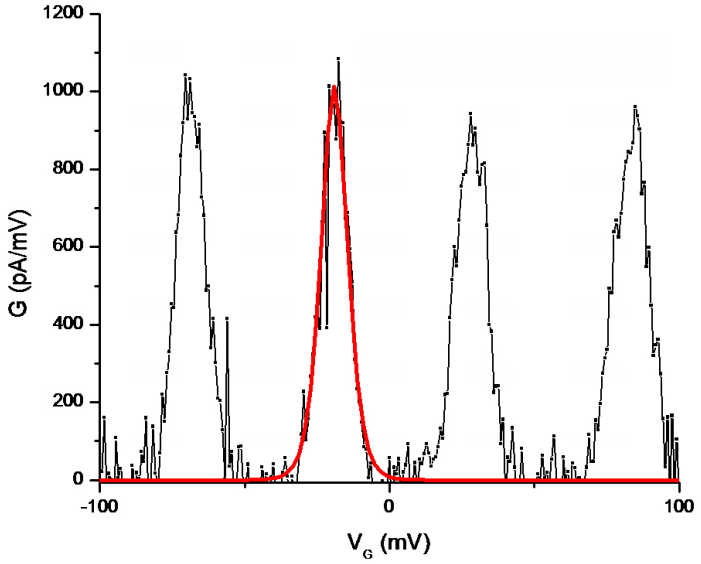

Figure 6.5: Black line corresponds to current vs gate voltage for sample no. 2 for small bias. The red line is a fit to theory, see Eq. 6.1. The agreement between the two is very good, although the temperature used for the fit is higher than the actual temperature.

6.2 Carbon Nanotube Double Quantum Dot

We first describe the double quantum dot formed on the nanotube and extract some of the relevant characteristics of the device from theory. We then

conclude with an attempt to use an SET situated about 22 μm away from the nanotube as a charge detector for the double dot. At room temperatures

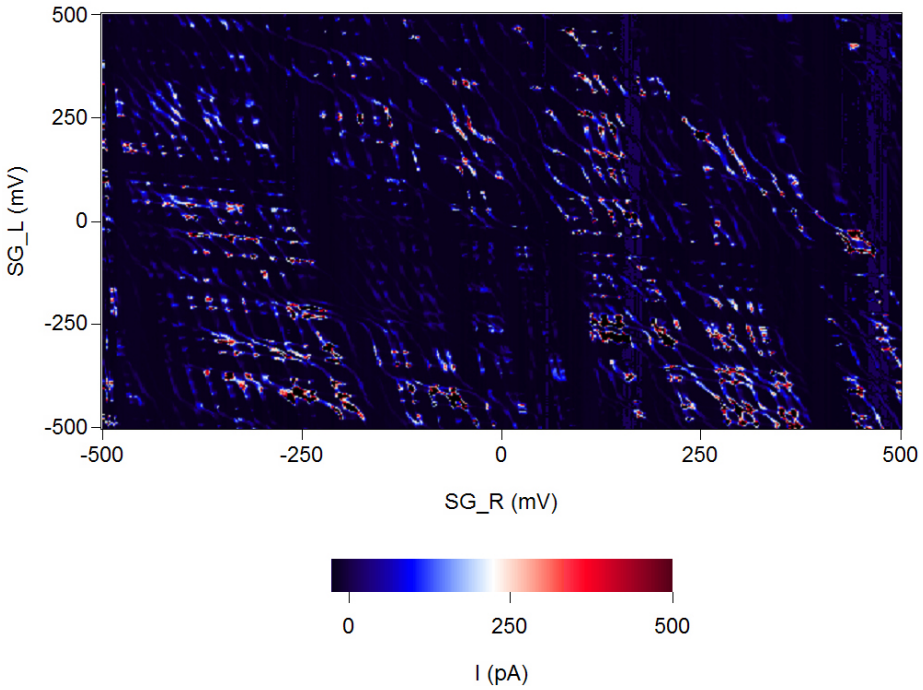

Figure 6.6: Current versus left and right side gate voltages for a 1 mV bias at 200 mK. Honeycomb patterns are clearly visible throughout the scanned region.

the working SET displayed a resistance of 300 kΩ while our working nanotube sample had a resistance of 150 kΩ. The nanotube segments forming the two dots are sized approximately 400 nm each. Sweeping both side gates SGL and SGR of the two dots and measuring the current we observe the appearance of honeycombs over a large energy range for a 1 mV bias, see Fig. 6.6. Cotunneling is also visible as a non-zero current away from the triple points. For a larger bias of 1.5 mV and proper values on the top gates to suppress cotunneling clear triangles appear together with clear excited states, see Fig. 6.7. In certain areas, with no magnetic field applied we observe two fold symmetry and it is also interesting to note that in a few areas there exist triangles with different base slopes, see Fig. 6.9, where probably another dot is also active somewhere in the system.

We proceed to characterize the double quantum dot according to theory. By reading off the vertical and horizontal dimensions of the honeycomb cell, ΔV_{SGL} and ΔV_{SGL}, the capacitances C_{SGL} and C_{SGR} are found through Eq. 3.12 to be $C_{SGR} = 6.6\ aF$, $C_{SGL} = 5.7$ aF respectively. By using Eq. 3.14 the voltage to energy conversion factors are extracted to be $\alpha_{SGR} = 0.27$ and $\alpha_{SGL} = 0.16$. The total single dot capacitances are then calculated to be $C_{\Sigma L} = 24$ aF, while $C_{\Sigma R} = 35$ aF. With these two last values in mind we read off the the vertical and horizontal voltage separation between the triple points of Fig. 6.10 and

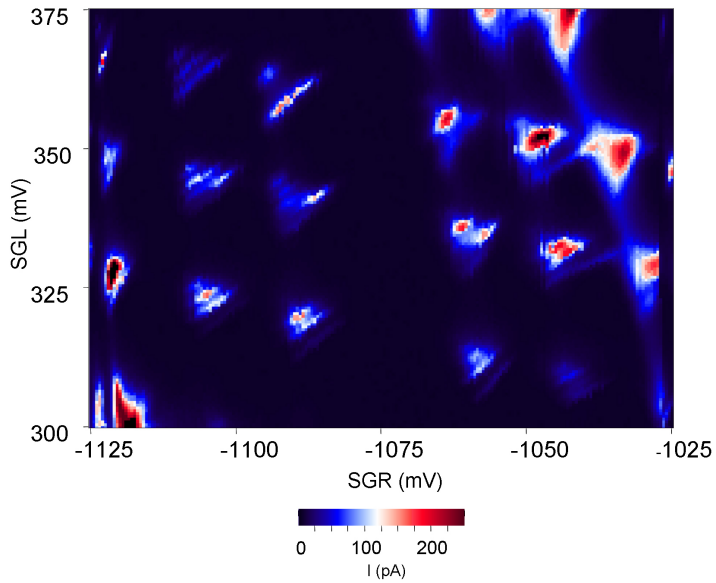

Figure 6.7: A zoom on some of the honeycombs. For values $V_{SD} = 1.5$ mV, TGM = 150 mV, TGL = 150 mV, TGR = 300 mV triangles and excited states are clearly visible while cotunneling is strongly supressed.

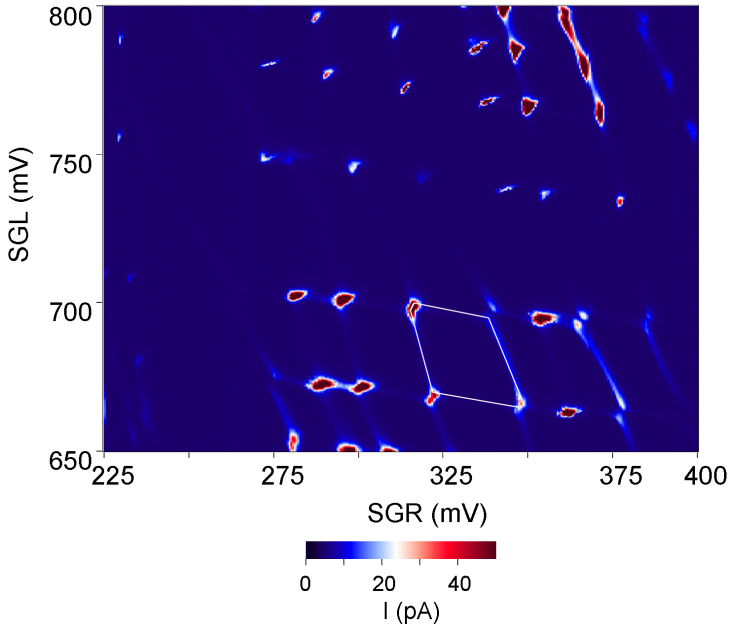

Figure 6.8: Zoom in on some of the honeycomb patterns for a bias voltage of 0.5 mV. The dimensions of the honeycomb outlined in white, ΔV_{SGR} and ΔV_{SGL}, were used to extract C_{SGR} and C_{SGL} respectively. We find $C_{SGR} = 6.6$ aF and $C_{SGL} = 5.7$ aF respectively.

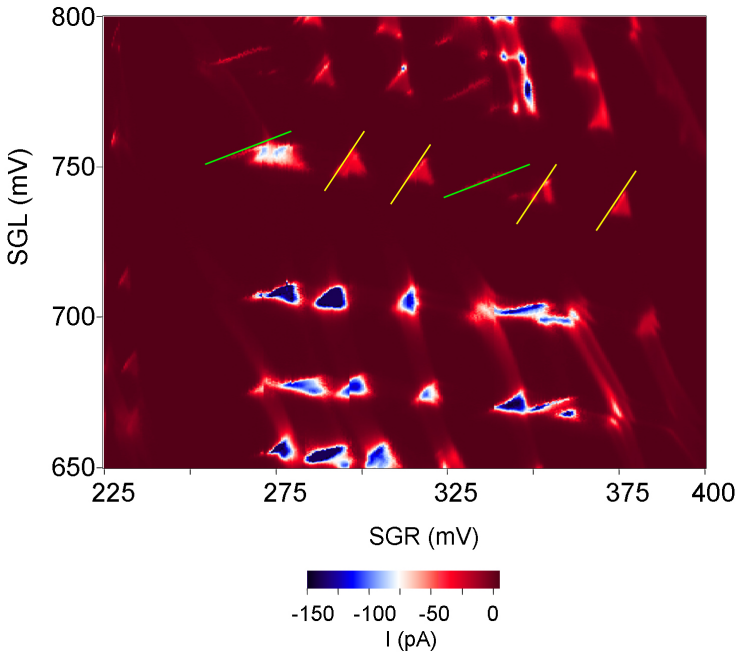

Figure 6.9: Zoom in on the honeycomb pattern for a bias voltage of -1.5 mV. Two groups of triangles, outlined in yellow and green, are observed with different slopes for their basis. Two fold symmetry is also observed for the triangles outlined in yellow.

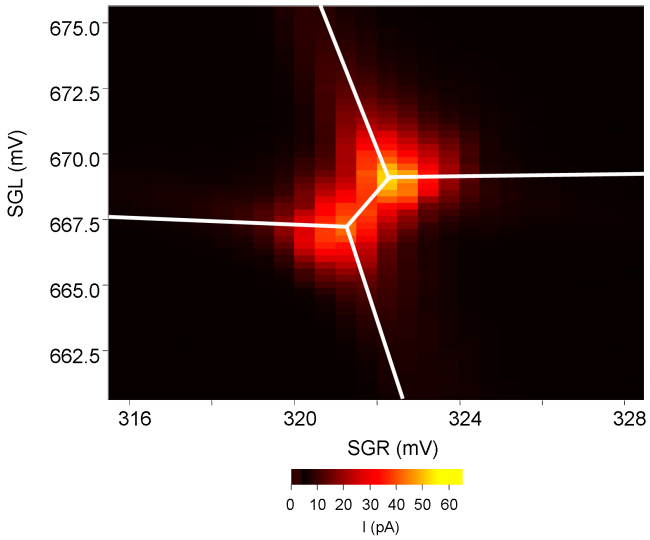

Figure 6.10: Zoom in on the bottom left corner of the honeycomb outlined in white in Fig. 3.13. The voltage offset in the vertical and horizontal direction between the two triple points can be used to extract C_m. We obtain a value of $C_m = 1.54$ aF.

plug everything in Eq. 3.13. We find a value of $C_m = 1.54$ aF. The capacitances between left dot and source, and right dot and drain are simply given by the remaining $C_L = 28.3$ aF and $C_R = 15,85$ aF respectively.

We next focus on a single area. Keeping the middle barrier, T_m, on zero we swept the bias voltage from 0.5 mV to -0.5 mV in 1 step. We fit the measured current trace at the middle of the triple points of Fig. 6.11(a) and Fig. 6.11(b). The lineshape is nicely fitted with a Lorentzian except for a small discrepancy on the absorption side.

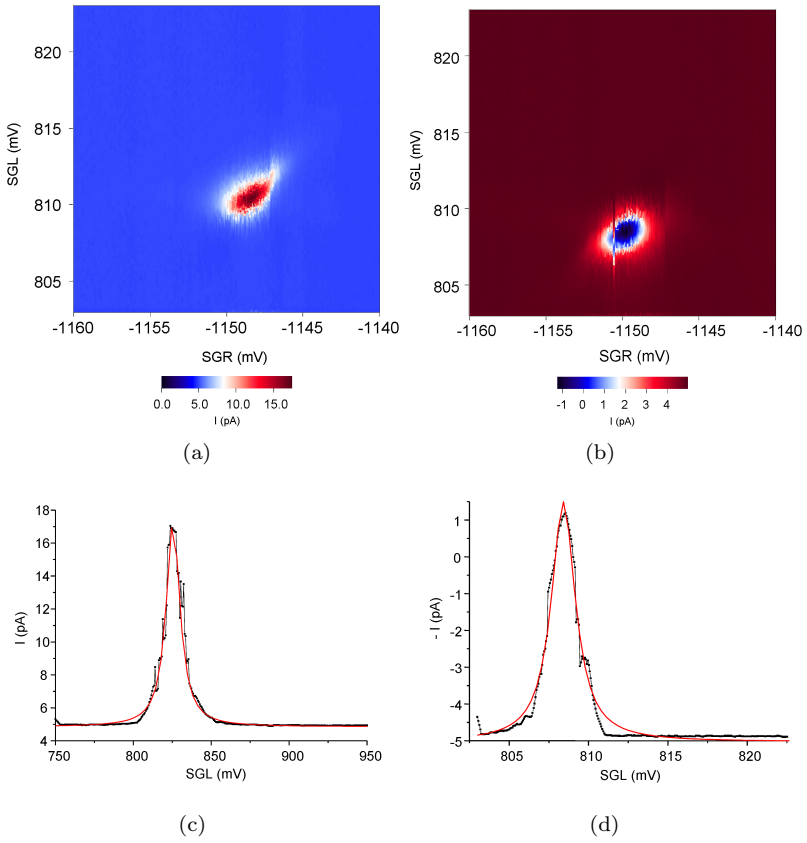

Figure 6.11: One pair of triple points for positive (Fig. 6.11(a)) and negative (Fig. 6.11(b)) bias of 0.5 mV and -0.5 mV respectively. Current lineshapes of (a) and (b) are plotted in Fig. 6.11(c) and Fig. 6.11(d). Fig. 6.11d appears inverted. The lineshapes can be fitted well by a Lorentzian [15].

From the maximum current and the width of the resonances for forward and backward bias one can extract all relevant parameters for the tunnel rates. Γ_1 stands for tunneling into the left dot from the source, Γ_3 for tunneling into the right dot from drain, and $|t_{12}|$ is the tunnel rate between the two dots.

We focus on the triple point depicted in Fig. 6.11. For larger bias the triple point evolves into a triangle. Fig. 6.12 was obtained for bias voltages of 1.5 mV and -1.5 mV respectively with the middle tunnel barrier on ground. We

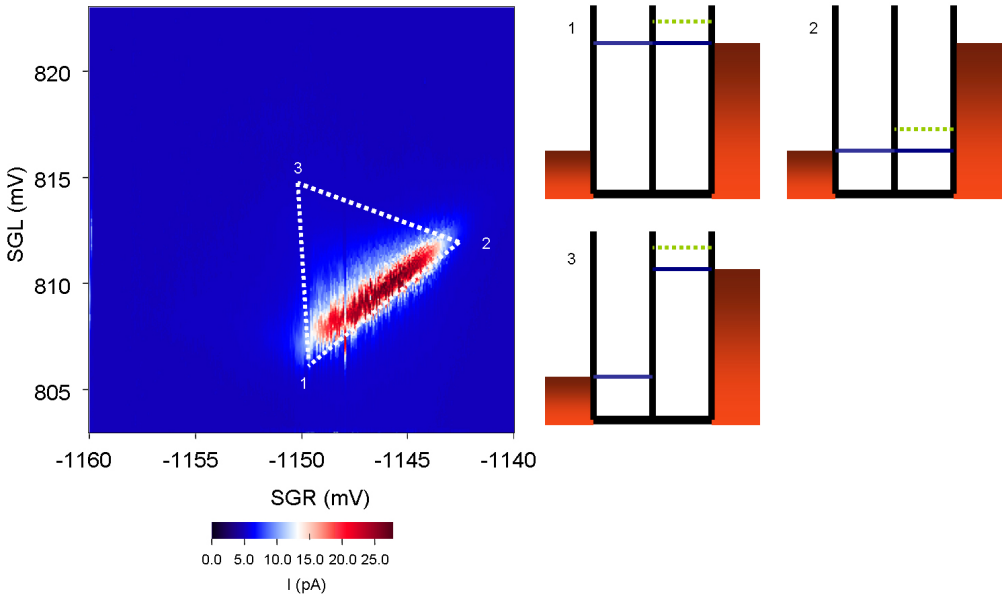

(a)

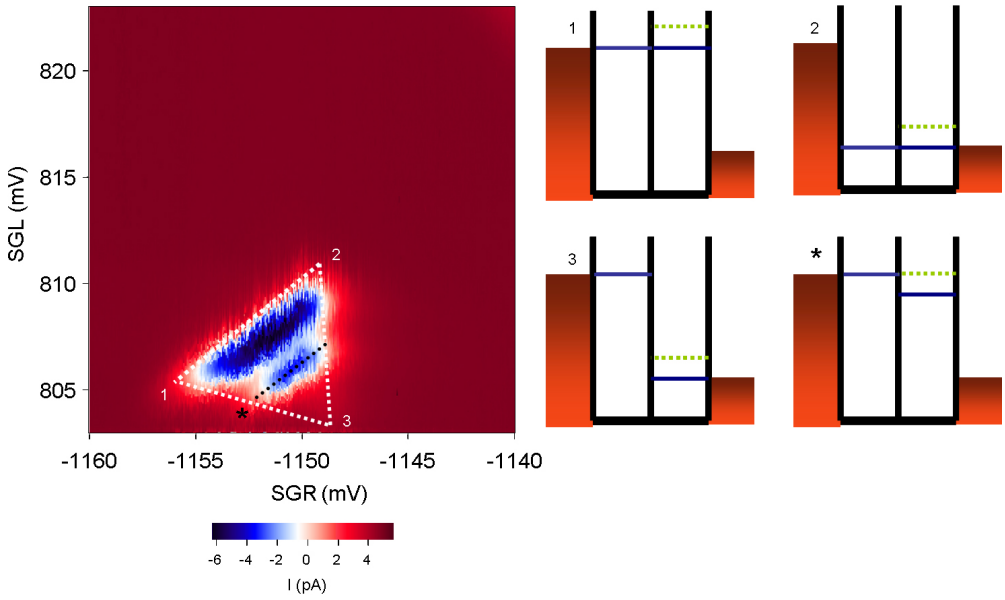

(b)

Figure 6.12: Top and bottom left: the triple point of Fig. 6.11 evolves into a triangle by application of a bias of 1.5 mV (top left) and -1.5 mV (bottom left) respectively. One excited state is visible in reverse bias but does not appear in forward bias. Top and bottom right: Schematic level configurations for the two dots that could explain the appearance of the excited state in reverse bias. Blue line denotes ground state transport, dashed yellow denotes excited state transport. For a more detailed description of all possibilities see text.

observe that one extra excitation comes in the transport window for negative bias but does not appear for positive bias. This excited state belongs to the right dot in accordance with Fig. 3.10(a). We assume n-type transport and extract possible level schemes in Fig. 6.12. We first examine Fig. 6.12b. Throughout the base of the triangle the ground states of the two dots are always aligned. In situation 2 the two ground states are aligned with the right lead and the resonant current is significant. Current through the excited state of the right dot is not possible since it lies higher in energy than the ground state of the left dot. As we move from situation 2 to 3 the voltage on the left gate, SGL, is decreased and therefore the ladder of the electrochemical potential of the right dot is shifted up. Initially the result is that the two ground states become misaligned so that current decreases. Only inelastic contributions to current remain. At some point however, denoted by $*$, the right dot excited state comes in resonance with the left dot ground state and current increases again. This increase in current is visible at $*$ and throughout the line that runs parallel to the base of the triangle since for all lines parallel to the base the electrochemical potentials of the two dots move in unison. Decreasing the side gate voltage SGL even further brings the left dot GS further up and away from the right dot excited state. An electron entering either the excited or the ground state of the right dot through the left lead is not in resonance either with the ground or excited state of the right dot anymore. Current therefore drops.

We then turn to the case of forward bias, see Fig. 6.12a. We proceed in the same way as above but start from situation 1. Here the two ground states are aligned with the right lead. To move from situation 1 to 3 the left side gate voltage, SGL has to be increased. This causes the left ground state to shift downwards. When this happens, an electron entering the right dot can only be tunnel inelastically to the left dot and current therefore drops. As the excited state of the left dot lies higher than the electrochemical potential of the right lead transport through it is not possible. In the same way, if we start from situation 2 and move towards situation 3 the left ground state will be pinned to the right lead while the electrochemical potential of the right dot will start shifting up. Although transport through the right dot excited state is possible since it is located in the transport window, it is never elastic and therefore current is low. Effectively, for forward bias the left dot lies for all possibilities at the same or lower value than the right dot ground state. The right dot excited state is thus always higher than the left dot ground state and will at best contribute to transport only inelastically. For this reason the right dot ES never comes in resonance with the left dot GS and thus it never shows up in transport under forward bias.

The coupled quantum dots can be modeled as a two-level system, in other words only one level in each dot is of significance as for instance two ground states. Then, transport through the system can occur in one of two ways: if the GSs are are aligned (resonant tunneling) the current is elastic as no energy is dissipated. When the two levels are misaligned there has to be some sort of medium that offers/receives the energy mismatch between the electrochemical potentials of the two dots. This medium could be for example photons (*Photon Assisted Tunneling*) or phonons.

In large bias triangles like the ones in Fig. 3.10(a) the elastic component of the current peaks at $\epsilon = 0$, that is, the elastic current peaks throughout the base of the triangle where the ground states are aligned. Finite current inside

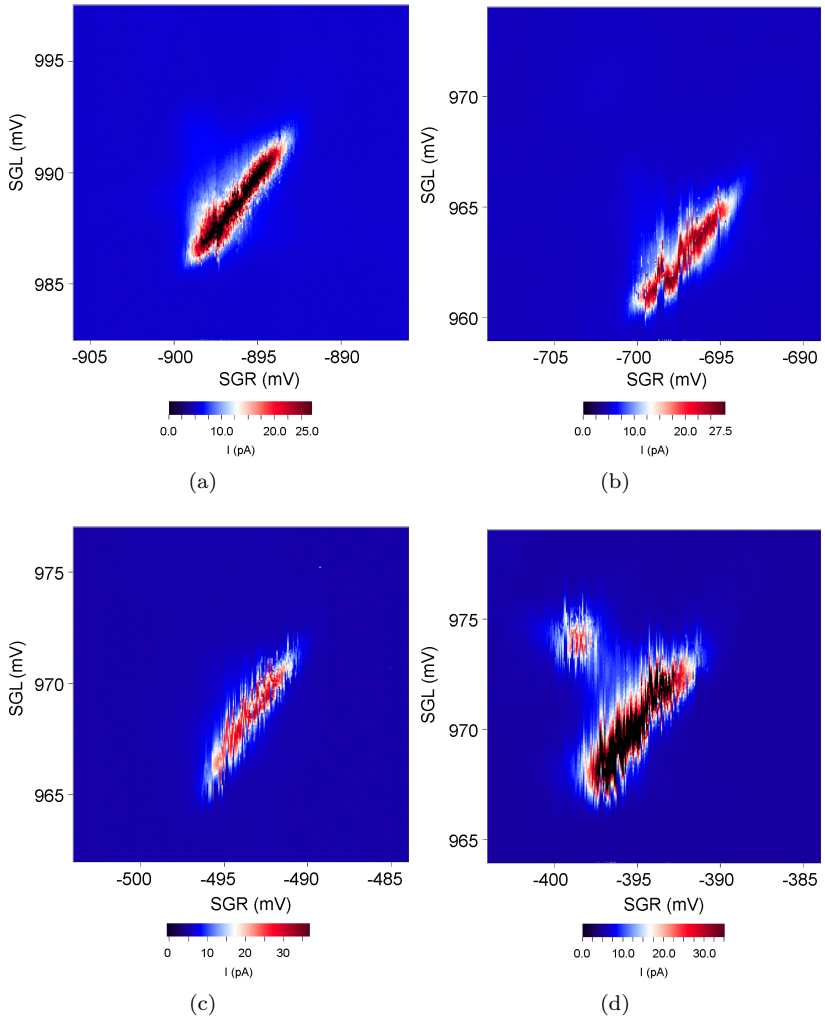

Figure 6.13: Zoom in on one pair of triangles at a bias of 1.5 mV. The two triangles fully overlap. The middle tunnel barrier TG_M is progressively changed from -200 mV (a) to -400 mV (b), -600 mV (c) and finally to -700 mV (d). One extra excitation appears at the top of the triangle at (d). The current linetraces are taken in the middle of the triangles and in parallel to the left side gate voltage SGL.

the triangles belongs to inelastic tunneling events. Theory predicts [16] that inelastic tunneling for a two level system such as our dots, coupled to a bosonic environment has a $|t_{12}|^2$ dependency. Therefore by tuning the tunnel barrier between the dots the inelastic current changes. If there exist modes of the bosonic environment that can affect transport they will show up as an increase in inelastic current.

We focus on one specific triangle and vary the middle barrier T_m in steps from 0 mV to -900 mV in an attempt to observe excited states mediating transport. This would generally show up as an overall increase in current as we move

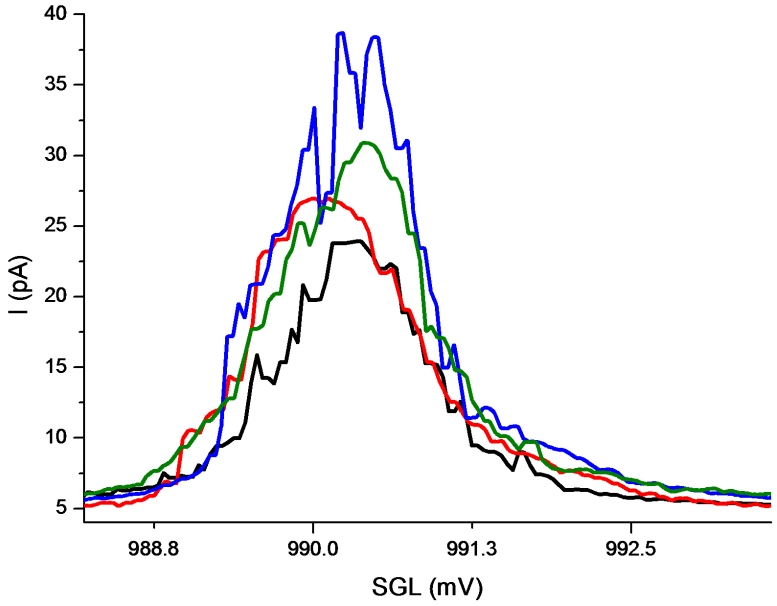

Figure 6.14: Current versus the side gate voltage SGL for the four situations depicted in Fig. 6.13. Different colors correspond to different values on the middle barrier TG_M. Black color corresponds to a value -200 mV, red to -400 mV, green to -600 mV, and finally blue to -700 mV on TG_M.

inside the triangles further away from the triangle base. In the ideal case that the modes of the bosonic environment are perfectly discrete and observable, the expected increase in current could come in discrete steps and would show up as additional lines running parallel to the triangle base as the middle barrier is varied. Fig. 6.13 shows that for a value of $TG_M = -700$ mV one excited state appears on the top of the triangle. This excited state is spaced approximately 5 meV from the ground state transition. We plot in Fig. 6.14 the current linetraces obtained for all four cases of Fig. 6.13. With the exception of the excited state mentioned above no other excited states are visible as no increase in overall inelastic current is observed by sweeping TG_M. The origin of the excited state of Fig. 6.13d remains undetermined as this honeycomb region shifted in the next measurements and could not be located again.

6.3 A Single Electron Transistor as a Charge Detector

We use an SET located 22 μm away from the nanotube as a charge sensor despite its significant distance from the dots. Without applying a magnetic field we varied the bias and gate voltage of the SET and measured the respective Coulomb diamond pattern in Fig. 6.15. As the diamonds are not fully closed

the SET is still in its superconducting state. We measured a charging energy of about 1.3 meV and a respective resistance of 300 kΩ as mentioned earlier. This value is roughly twice what we expect for our oxidation time. Compared to our test structures this SET shows somewhat poorer characteristics.

To check how strongly the left (SGL) and right (SGR) side gates couple to the SET we compare them to the actual SET side gate. We first vary SGL and then SGR from -1000 mV to 1000 mV respectively, while biasing the SET at 100 μV, see Fig. 6.16.

Comparing the number of Coulomb peaks in each case for the same energy range we conclude that SGL is still coupled to the SET, 81% as much as the actual SET gate. SGR however seems to be minimally coupled as in the energy range we measured only half a Coulomb oscillation was recorded. We speculate that this is due to the position of SGR on the wafer: SGL, and the line connecting it to the contact pads screens the SET completely from SGR. Without

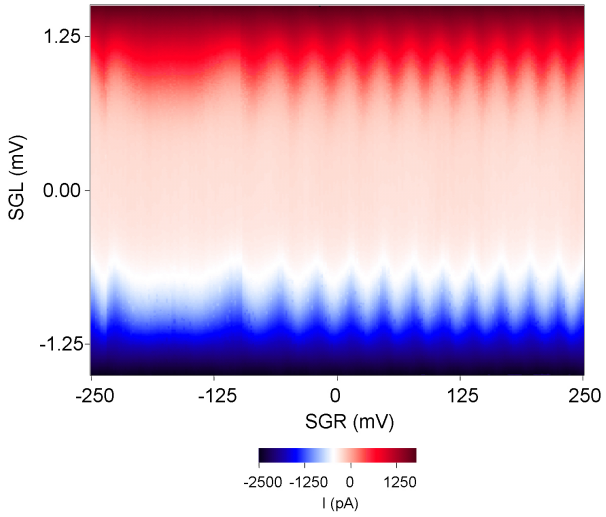

Figure 6.15: Current versus SET bias and side gate voltages obtained at 70 mK. The SET appears to be still in the superconducting state.

putting voltages on the dot barriers, we biased the SET at 100 μV and the nanotube at 500 μV respectively. We first swept the left side gate SGL from -1 V to +1 V, and then the right side gate SGR in the same range as SGL.

We simultaneously measure the sharp current peaks through the nanotube and the SET as a function of the left nanotube side gate SGL, see Fig. 6.17, and compare the voltages at which nanotube current peaks occur to the respective voltage values on the SET Coulomb peaks. At a first glance no real charge sensing is observed: for the voltage values where the nanotube coulomb oscillations occur the SET's Coulomb peaks are not significantly affected as we would expect from theory. No clear distortion of the SET peaks is observed neither in the bottom/top parts of the peaks were the phenomenon would be weakest, nor, most importantly, halfway up the peaks at their most sensitive area.

By zooming in more closely in Fig. 6.18 we see that although certain tunneling events on the tube coincide with small distortions of the Coulomb peaks,

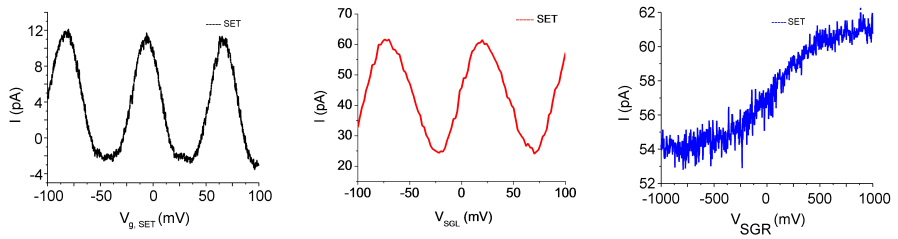

(a) (b) (c)

Figure 6.16: SET Coulomb peaks as a function of SET side gate (a), carbon nanotube left side gate SGL (b) and carbon nanotube right side gate SGR (c). Note that SGL is only somewhat less coupled to the SET than the SET side gate, while SGR seems to be minimally coupled. In (a) the SET is biased at 50 μV while for (b) and (c) the SET bias is 100 μV.

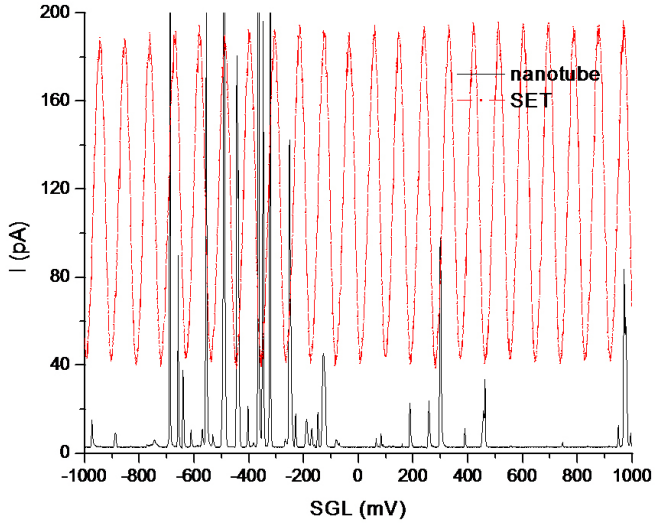

Figure 6.17: Charge sensing attempt while sweeping SGL. Sharp peaks (black) correspond to the nanotube while Coulomb oscillations (red) to the SET. The SET measurement is magnified by (x6) and shifted vertically for clarity. A zoom in on one of the oscillations is displayed in Fig. 6.18.

these distortions are in fact rather weak. There are also numerous cases where distortions in the SET peak heights do not coincide with actual tunneling events in the nanotube and therefore it appears that without *compensation* the SET cannot act as a charge sensor. A number of factors could be limiting the charge sensing capability of our SET: a) the SET is too far away from the tube, b) our SET quality is not optimum as our test structures, c) the SET is sensitive to electrostatic switching events in the environment other than the tube, and d) the noise from our setup, particularly the pumps, also could contribute to

non-clear SET Coulomb peaks. Finally, it seems the most important factor

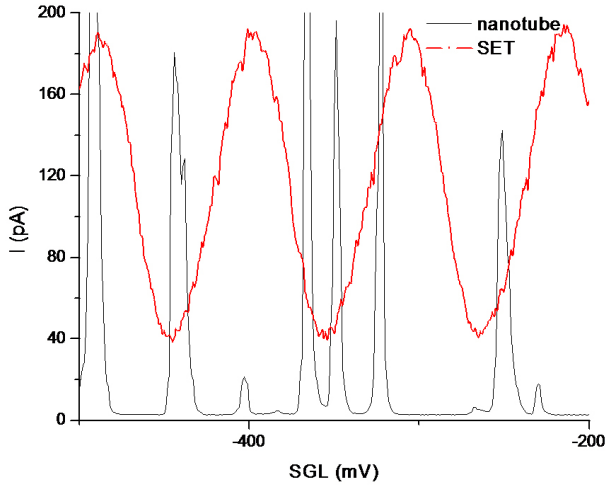

Figure 6.18: Zoom in one of the areas of Fig. 6.17. Even halfway up the SET Coulomb peaks where sensitivity is maximum there is no significant change in the peaks due to simultaneous tunneling events on the tube (black). No charge sensing is observable.

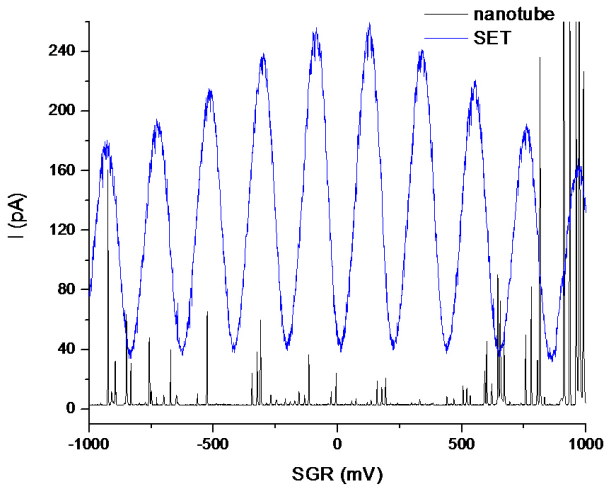

Figure 6.19: Charge sensing attempt while sweeping SGR. Sharp peaks (black) correspond to the nanotube while Coulomb oscillations (blue) to the SET. SET measurements are magnified and shifted vertically for clarity.

limiting charge sensing is the stray capacitance of the long side gate metal line

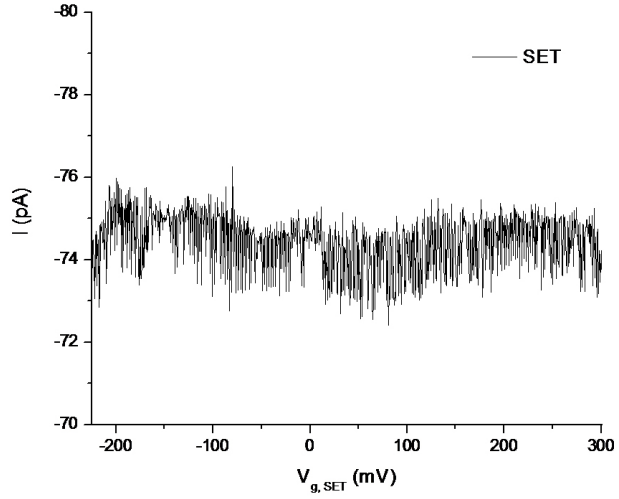

Figure 6.20: SET current trace while sweeping the nanotube left side gate (SGL) and in reverse the SET side gate. The different coupling between the two to the SET is taken into account. The SET current remained constant thus displaying compensation although no charge sensing is found.

connecting it to the contact pads. The size and position of this line is such that the SET predominantly senses the voltage on it rather than any voltage on the nanotube.

We bias the SET at its points of highest sensitivity: halfway up a Coulomb peak to perform *compensation*. To this end we sweep the voltage on the tube SGL and simultaneously vary the voltage on the SET gate in reverse direction, with values 0.81 smaller than those on SGL to compensate, see Fig. 6.20. The current trace remains constant over a large energy range. Thus, our compensation attempt is successful at keeping the current pinned. However, no current sawtooth characteristics are visible and therefore charge detection proved in total to be unsuccessful in this particular device even with charge compensation.

Chapter 7

Conclusions

The first goal of this project was to reproducibly fabricate Single Electron Transistors. The second goal was to fabricate Carbon Nanotube Double Quantum Dots and the final objective was to use the SET as a charge sensor on carbon nanotube double dots to extract stability diagrams and relevant relaxation times. Based on our work the following conclusions can be drawn.

- Single Electron Transistors have been reproducibly fabricated. All the relevant tunable parameters are under our experimental control.
- Narrow top gated Carbon Nanotube Double Quantum Dots have been fabricated and characterized according to theory.
- Single Electron Transistors have been fabricated together with Carbon Nanotube Double Quantum Dots.
- We observe carbon nanotube double quantum dot excited states.
- Our attempt to vary the middle tunnel barrier and observe increased inelastic contribution to the current was inconclusive. Although one excited state appears at large negative values of the middle barrier, its origin is unclear.
- Our attempt to use an SET located far away from the double dots as a charge sensor was unsuccessful. Compensation was however successful.
- For charge sensing, Single Electron Transistors need to be not further than a few μm from the double dot. For SETs that are located further it would be useful to extend the SET island closer to the dots through the fabrication of an antenna so that the coupling is better.
- The design for such structures should be such that stray capacitances are not dominant in determining the SET current signal.

Bibliography

[1] Erlingsson S. and Nazarov Y., *Hyperfine-mediated transitions between a Zeeman split doublet in GaAs quantum dots: The role of the internal field*, Physical Review B **66**, 155327 (2002).

[2] Dresselhaus M. and Eklund P., *Phonons in carbon nanotubes*, Advances in Physics **49**, 705 (2000).

[3] Dekker C., *Carbon Nanotubes as Molecular Quantum Wires*, Physics Today, May 1999.

[4] Tans S. et al., *Room-temperature transistor based on a single carbon nanotube*, Nature **393**, 49 (1998).

[5] Avouris Ph. et al., *Electrically Induced Optical Emission from a carbon nanotube*, Science **300**, 783 (2003).

[6] Sapmaz S., Meyer C. et al., *Excited States Spectroscopy in Carbon Nanotube Double Quantum Dots*, cond-mat **/0602424**, (2006).

[7] Jing Kong, *Carbon Nanotubes: Synthesis, Integration and Properties*, Phd Dissertation, Stanford University, (2002).

[8] Avouris Ph. et al., *Molecular Electronics with Carbon Nanotubes*, Accounts of Chemical Research **35**, No. 12, 1027 (2002) Cambridge, England (1995).

[9] Minot. D. Ethan, *Tuning the Band Structure of Carbon Nanotubes*, PhD Dissertation, Cornell University (2004).

[10] Dresselhaus M., Dresselhaus G. and Eklund P., *Science of Fullerenes and Carbon Nanotubes*, Academic Press (1996).

[11] Babic B., *Electrical Characterization of Carbon Nanotubes grown by the Chemical Vapor Deposition Method*, Phd Inauguraldissertation, Universität Basel, (2004).

[12] Sapmaz S., Jarillo-Herrero P. et al., *Electronic excitation spectrum of Metallic carbon Nanotubes*, Physical Review **B**, 153402 (2005).

[13] van der Wiel W., *Electron transport through double quantum dots*, Reviews of Modern Physics **75**, No.1, 1-22 (2003).

[14] Naber W., *Spin dependent transport in few electron laterally coupled double quantum dots*, Master Thesis, TUDelft (2004).

[15] van der Vaart N. et al., *Resonant Tunneling through two discrete energy states*, Physical Review Letters **74**, No.23, 4702 (1995).

[16] Leggett A. et al., *Dynamics of the dissipative two-state system*, Reviews of Modern Physics **59**, Issue 1, 1-85 (1987).

[17] Ashoori R. et al., *Single-electron transistor as a charge sensor for semiconductor applications*, Journal of Vacuum Science and Technology **B 15(6)**, 2844 (1997).

[18] Bühler M., Brenner R. et al. *Single-electron transistor architectures for charge detection in solid-state quantum computer devices*, Smart Materials and Structures **11**, 740-755 (2002).

[19] Hadley P., *Single Electron Transistors*, Institute of Physics Conference Series **174**, Compound Semiconductors 2002, Proceedings of the 29th International Symposium, Lausagne, 125-132 (2002).

[20] Devoret M. and Schoelkopf. R, *Amplifying quantum signals with the single-electron transistor*, Nature **406**, 1039 (2000).

[21] Brenner Rolf, *Single Electron Transistors for detection of charge motion in the solid state*, PhD Dissertation, The University of New South Wales (2004).

[22] Hadley P., Visscher E. et al., *3e tunneling processes in a superconducting single-electron tunneling transistor*, Physical Review B **58**, No.23, 15317 (1998).

[23] Cyrot M. and Pavuna D., *Introduction to Superconductivity and High-Tc Materials*, World Scientific Publishing (1990).

[24] van Houten H., Beenakker C. et al., *Coulomb-Blockade Oscillations in Semiconductor Nanostructures*, Solid State Physics **44**, 1-228 (1991).

[25] Biercuk M. et al., *Charge Sensing in carbon nanotube quantum dots on microsecond timescales*, cond-mat/0510550v1, (2005).

[26] Gräber M. et al., *Molecular States in Carbon Nanotube Double Quantum Dots*, cond-mat/0603367v1 (2005).

[27] Mason N. et al., *Local Gate Control of a Carbon Nanotube Double Quantum Dot*, Science **303**, 655 (2004).

[28] Petta J. et al., *Manipulation of a Single Charge in a Double Quantum Dot*, Physical Review Letters **93**, No.18, 186802 (2004).

[29] Fujisawa T. et al., *Spontaneous Emission Spectrum in Double Quantum Dot Devices*, Science **282**, 932 (1998).

[30] Fujisawa T. et al., *Electrical pulse measurements, inelastic relaxation, and non-equilibrium transport in a quantum dot*, Journal of Physics: Condensed Matter **15**, R1395-R1428 (2003).

[31] Kouwenhoven L.P. et al., *Electron Transport in Quantum Dots*, Advanced Study Institute on Mesoscopic Electron Transport, Kluwer (1997).

Appendix A

Electrostatic energy of quantum dot systems

We present a derivation of the electrostatic energy of quantum dot systems. We first start by briefly discussing the method employed for solving the electrostatics.

A.1 Electrostatics of a system of N conductors

Let there be a system of N conductors. For each conductor we can define one capacitance connecting it to ground and another (N-1) capacitances connecting it to the rest of the conductors in the system. This results in a total of N(N+1)/2 capacitors. The total charge of one of these conductors is then the sum of the charges on all the capacitors connected to it

$$Q_j = \sum_{k=0}^{N} q_{jk} = \sum_{k=0}^{N} c_{jk}(V_j - V_k) \tag{A.1}$$

where V_j is the electrostatic potential of conductor j, c_{jk} the respective capacitance connecting conductor j to conductor k, and $V_0 = 0$ the potential on ground. The above equation can be expressed more compactly in matrix form as

$$\overrightarrow{Q} = \mathbf{C}\overrightarrow{V} \tag{A.2}$$

where $\mathbf{C}$ is the so-called *capacitance matrix*, $\overrightarrow{Q}$ a vector containing the charges on all conductors and $\overrightarrow{V}$ a vector with the individual potentials on every conductor. A diagonal element of the capacitance matrix contains the sum of all capacitances of this conductor to all the rest in the system

$$C_{jj} = \sum_{k=0, k\neq_j}^{N} c_{jk} \tag{A.3}$$

For instance for a system of three conductors $C_{11} = C_{01} + C_{12} + C_{13}$. An off-diagonal element of the capacitance matrix is minus the capacitance between

conductor j and conductor k, or $C_{jk} = C_{kj} = -c_{jk}$. The electrostatic energy of the system of N(N+1)/2 capacitors then has a total energy given by

$$U = \frac{1}{2}\overrightarrow{V}\mathbf{C}\overrightarrow{V} = \frac{1}{2}\overrightarrow{V}\overrightarrow{Q} = \frac{1}{2}\overrightarrow{Q}\mathbf{C}^{-1}\overrightarrow{Q} \tag{A.4}$$

For a more realistic network voltage sources also have to be included. They can be treated as nodes with large capacitances to ground and large charges on them.

A.2 Single Quantum Dots

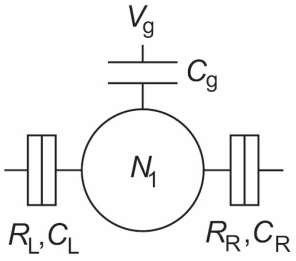

Figure A.1: A schematic representation of a quantum dot circuit. The dot is coupled capacitatively to source (L), drain (R) and a nearby gate (G). Particle exchange occurs only through tunneling from the leads.

The total charge Q_1 on the dot can be written as the sum of the charges on all capacitors connected to the dot

$$Q_1 = C_L(V_1 - V_L) + C_G(V_1 - V_G) + C_R(V_1 - V_R) \tag{A.5}$$

$$Q_1 + C_L V_L + C_G V_G + C_R V_R = C V_1 \tag{A.6}$$

with $C = C_L + C_R + C_G$ the total dot capacitance. Using Eq. A4 and substituting $Q_1 = -(N_1 - N_0)|e|$ we obtain

$$U(N_1) = \frac{[-(N_1 - N_0)|e| + C_L V_L + C_R V_R + C_G V_G]^2}{2C} \tag{A.7}$$

If we take into account quantum mechanics and add the single particle energies to the above formula we end up with Eq. 3.3.

A.3 Double Quantum Dots

We write the total charge $Q_{1(2)}$ on dot 1(2) as the sum of the charges on all the capacitors connected to dot 1(2), see Fig. A.2.

$$Q_1 = C_L(V_1 - V_L) + C_{G1}(V_1 - V_{G1}) + C_m(V_1 - V_2) \tag{A.8}$$

$$Q_2 = C_R(V_2 - V_R) + C_{G2}(V_2 - V_{G2}) + C_m(V_2 - V_1) \tag{A.9}$$

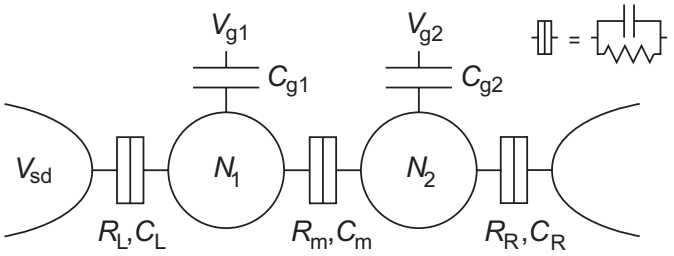

Figure A.2: A double quantum dot modeled as a network of resistors and capacitances. The dots are represented by the two circles with $N_{1(2)}$ electrons on dot 1(2). The dots are coupled to the leads by a resistor $R_{L(R)}$ and a capacitor $C_{L(R)}$ and to each other by a resistor R_m and a capacitor C_m. Two gate voltages $V_{g1(2)}$ are coupled to the dots through capacitances $C_{g1(2)}$.

This can be rewritten as

$$\begin{pmatrix} Q_1 + C_L V_L + C_{G1} V_{G1} \\ Q_2 + C_R V_R + C_{G2} V_{G2} \end{pmatrix} = \begin{pmatrix} C_1 & -C_m \\ -C_m & C_2 \end{pmatrix} \begin{pmatrix} V_1 \\ V_2 \end{pmatrix} \tag{A.10}$$

where $C_{1(2)} = C_{L(R)} + C_{G1(2)} + C_m$ The charge on each dot is $Q_{1(2)}{=}{-}N_{1(2)}|e|$.

Then according to Eq. A.4 the electrostatic energy reads

$$\begin{aligned} U(N_1,N_2) &= \frac{1}{2}N_1E_{c1} + \frac{1}{2}N_2E_{c2} + N_1N_2E_{cm} + \\ &\quad + f(V_{G1},V_{G2}) + g(V_L,V_R) + h(V_{G1},V_{G2},V_L,V_R) \\ f(V_{G1},V_{G2}) &= \frac{1}{e}[C_{G1}V_{G1}(N_2E_{cm}+N_1E_{c1}) + C_{G2}V_{G2})N_1E_{cm} + N_2E_{c2}] \\ &\quad + \frac{1}{e^2}[\frac{1}{2}C_{G1}^2V_{G1}^2E_{c1} + \frac{1}{2}C_{G2}V_{G2}E_{c2} + C_{G1}C_{G2}V_{G1}V_{G2}E_{cm}] \\ g(V_L,V_R) &= \frac{1}{e}[C_LV_L(N_2E_{cm}+N_1E_{c2}) + C_RV_R(N_1E_{cm}+N_2E_{c2}] + \\ &\quad + \frac{1}{e^2}[\frac{1}{2}C_L^2V_L^2E_{c1} + \frac{1}{2}C_R^2V_R^2E_{c2} + C_LC_RV_LV_RE_{cm}] \\ h(V_{G1},V_{G2},V_L,V_R) &= \frac{1}{e^2}[C_LV_LC_{G1}V_{G1}E_{c1} + C_RV_RC_{G2}V_{G2}E_{c2} + \\ &\quad + C_LV_LC_{G2}V_{G2}E_{cm} + C_RV_RC_{G1}V_{G1}E_{cm}] \end{aligned} \tag{A.11}$$

The charging energies E_{c1}, E_{c2} as well as the coupling energy E_{cm} are given as

$$\begin{aligned} E_{C1} &= \frac{e^2}{C_1}\left(\frac{1}{1-\frac{C_m^2}{C_1C_2}}\right) \\ E_{C2} &= \frac{e^2}{C_2}\left(\frac{1}{1-\frac{C_m^2}{C_1C_2}}\right) \\ E_{Cm} &= \frac{e^2}{C_m}\left(\frac{1}{\frac{C_1C_2}{C_m^2}-1}\right) \end{aligned} \tag{A.12}$$

They are exactly the same as those given in Chapter 3.2. For the case of $V_L = V_R = 0$ and $Q_{1(2)} = -N_{1(2)}|e|$ the total energy then reads

$$U(N_1, N_2) = \frac{1}{2}N_1^2 E_{C1} + \frac{1}{2}N_2^2 E_{C2} + N_1 N_2 E_{Cm} + f(V_{g1}, V_{g2}) \tag{A.13}$$

$$f(V_{g1}, V_{g2}) = \frac{1}{e}\{C_{g1}V_{g1}(N_1 E_{C1} + N_2 E_{Cm}) + C_{g2}V_{g2}(N_1 E_{Cm} + N_2 E_{C2})\} \tag{A.14}$$